

Electrochemical signatures in proton exchange membrane fuel cells: A comprehensive study based on distribution of relaxation times

Original

Electrochemical signatures in proton exchange membrane fuel cells: A comprehensive study based on distribution of relaxation times / Mazzeo, Francesco; Di Napoli, Luca; Carello, Massimiliana; Prokop, Martin; Paidar, Martin; Bouzek, Karel. - In: INTERNATIONAL JOURNAL OF HYDROGEN ENERGY. - ISSN 0360-3199. - ELETTRONICO. - 202:(2026). [10.1016/j.ijhydene.2025.152860]

Availability:

This version is available at: 11583/3006645 since: 2026-01-16T11:58:31Z

Publisher:

Elsevier

Published

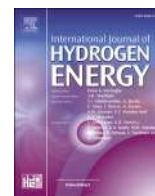
DOI:10.1016/j.ijhydene.2025.152860

Terms of use:

This article is made available under terms and conditions as specified in the corresponding bibliographic description in the repository

Publisher copyright

(Article begins on next page)



Electrochemical signatures in proton exchange membrane fuel cells: A comprehensive study based on distribution of relaxation times

Francesco Mazzeo^{a,*}, Luca Di Napoli^b, Massimiliana Carello^a, Martin Prokop^c,
Martin Paidar^c, Karel Bouzek^c

^a Politecnico di Torino, Turin, Italy

^b Eaton European Innovation Center (EEIC), Roztoky, Czech Republic

^c University of Chemistry and Technology (UCT), Prague, Czech Republic

ARTICLE INFO

Keywords:

Polymer electrolyte membrane fuel cell (PEMFC)
Electrochemical impedance spectroscopy (EIS)
Distribution of relaxation times (DRT)
Operating parameter effects
Peaks interpretation

ABSTRACT

The impedance response of a proton exchange membrane fuel cell (PEMFC) was analyzed using the Distribution of Relaxation Times (DRT) under varied operating conditions of load, temperature, pressure, stoichiometry, and oxidant type. Six relaxation processes were identified and characterized through their resistance and time constant evolution. A non-linear regression framework quantified their statistical significance and correlations with operating parameters, while reconstruction errors and confidence intervals revealed non-negligible uncertainties affecting interpretation. The highest-frequency contribution appears mainly as a DRT regression artifact, though its resistance still exhibits temperature dependence, possibly linked to proton transport or residual ohmic effects. Among the remaining high-frequency features, one is statistically insignificant, while another shows mixed dependencies, suggesting the superposition of multiple concurrent processes. Mid- and low-frequency contributions vary coherently with temperature, pressure, and load, consistent with charge-transfer and mass-transport phenomena. Overall, the work establishes a quantitative link between operating parameters and internal processes, advancing the diagnostic and predictive capabilities of DRT for PEMFCs.

1. Introduction

The problem of climate change has led, over the past decades, to a paradigm shift regarding energy supply sources. Renewable energy sources are increasingly being used to meet the targets of limiting temperature rise defined in the “Paris Agreement” in 2015 [1]. In this context, hydrogen plays a crucial role as an energy vector to compensate for the intermittency of renewable energy sources. Additionally, it is attractive for large-scale grid storage due to its high gravimetric energy content (143 MJ kg^{-1}) [2]. PEMFCs convert the chemical energy of hydrogen into electricity with high efficiency, around 50 % at nominal power (0.6 V , 2.67 A/cm^2) [3], and zero carbon dioxide emissions during operation, a key advantage for the transportation sector, where real-world energy demand is steadily increasing [4,5]. Owing to their rapid startup and ability to handle high-power demands, PEMFCs are particularly well suited for hydrogen-powered mobility, especially in heavy-duty transport. They help bridge the gap between Internal Combustion Engine vehicles (ICEs) and Battery Electric Vehicles (BEVs) [6]

and are often combined with the latter to smooth out variable on-road loads [7]. However, full PEMFC entry into the market is currently limited by costs and the durability of the system. For these reasons, understanding the internal processes occurring within PEMFCs is critical for optimizing their performance and diagnosing potential faults. EIS is an online diagnostic method that provides information on the internal impedance of the cell, using perturbation current or voltage signals at different frequencies around its steady-state and measuring system response [8]. Generally, information about internal resistances is obtained by fitting the experimental impedance spectrum with Equivalent Circuit Models (ECMs) that represent the physics of the electrochemical cell [8–10], a modeling approach that is also widely applied in other fields [11]. However, not all theoretically expected internal processes are always present in an experimental impedance spectrum, and the non-linear regression used for fitting is highly sensitive to the initial guesses chosen for the ECM parameters [8,12,13]. A complementary methodology for analyzing experimental impedance spectra, which has become increasingly popular in recent years, is the Distribution of

* Corresponding author.

E-mail address: francesco.mazzeo@polito.it (F. Mazzeo).

<https://doi.org/10.1016/j.ijhydene.2025.152860>

Received 6 June 2025; Received in revised form 10 November 2025; Accepted 30 November 2025

Available online 16 December 2025

0360-3199/© 2025 The Authors. Published by Elsevier Ltd on behalf of Hydrogen Energy Publications LLC. This is an open access article under the CC BY license (<http://creativecommons.org/licenses/by/4.0/>).

Relaxation Times (DRT). This approach has been applied to various electrochemical systems to study degradation and performance, including batteries [14–16], solid oxide fuel cells [10,17,18] and PEMFCs [19,20]. The concept behind this approach is to deconvolute the measured complex impedance as the sum of an ohmic resistance and an infinite series of Voigt circuits, each associated with a specific relaxation time constant. In an ideal system, each process would appear as a Dirac delta function at its characteristic frequency, whereas in real systems, the interdependence of phenomena broadens this response into a distributed spectrum of electrochemical intensities. This method is not strictly applicable to systems dominated by semi-infinite diffusion, such as batteries or supercapacitors, which exhibit a Warburg-type impedance with a constant 45° phase angle [21–23]. In PEMFCs, the oxygen reduction reaction (ORR) is strongly coupled with oxygen and proton diffusion within the catalyst layer, giving rise to a partial 45° trend in the high-frequency region of the Nyquist plot. Nonetheless, DRT analysis remains suitable, as proton transport often deviates from ideal Warburg behavior due to non-uniform conductivity linked to water generation [24]. Moreover, the dominant faradaic ORR response typically masks the 45° diffusion behavior, while oxygen bounded diffusion appears instead as a depressed arc that can be effectively modeled by a parallel RC element. The DRT for PEMFC has been used for multiple reasons in the literature. Recently, Artigas et al. [19] applied this technique as a means of water management in an industrial stack. Bevilacqua et al. [20], used DRT to analyse the performance of High Temperature (HT) PEMFC with different catalysts. Han et al. [25], used DRT to analyse the performance of a low-temperature (LT) PEMFC at varying current, temperature and relative humidity, differentiating the various contributions of the electrochemical reaction through peak analysis. Ao et al. [26] applied the DRT to analyse a PEMFC stack under various operating conditions, providing demonstration of its diagnostic capabilities, particularly regarding water transport.

Despite its increasing adoption, the DRT interpretation still relies on *a priori* assumptions, potentially leading to erroneous conclusions if the underlying processes are not correctly identified.

1.1. DRT methodology overview

The DRT expresses the measured impedance as a continuous function of the logarithmic time constant distribution. Since EIS frequencies are typically logarithmically spaced, the time distribution is conveniently represented in logarithmic form, as shown in Eq. (1).

$$Z_{DRT}(f) = R_{\infty} + \int_{-\infty}^{\infty} \frac{\gamma(\ln(\tau))}{1 + i2\pi f\tau} d\ln(\tau) \quad (1)$$

Where R_{∞} is the ohmic resistance, $\gamma(\ln(\tau))$ is a suitable function that describes the logarithmic distribution of time constants, f is the frequency and τ is the time constant.

In practice, only a finite number of frequency points are available from EIS measurements, defined by the selected points per decade. As a result, the logarithmic timescale distribution must be discretized over a finite range to enable numerical deconvolution. Since the fitting of Z_{DRT} to experimental data is an ill-posed problem, Tikhonov regularization is commonly applied to ensure a stable and physically meaningful solution. This method introduces a penalty term, controlled by the parameter λ , which balances the trade-off between fitting accuracy and smoothness. A small λ preserves resolution but amplifies noise, whereas a large one over-smooths the distribution. The optimal value of λ is typically determined via cross-validation or the L-curve criterion [27, 28], yielding different optimal ranges depending on the criterion used [27,29], although visual inspection remains essential to avoid losing relevant physical features. No universal value exists, as optimal regularization depends on the system, the measurement setup, and the test conditions [30]. In this work, values in the range from 10^{-5} to 10^{-4} were adopted, ensuring robust parameter extraction and consistency with

prior studies [19,25,31]. A statistical analysis was further employed to confirm the significance of the identified peaks, so that the conclusions are not affected by the specific choice of λ . The penalty term used is the square of the norm of the first derivative or second derivative of the DRT function, while the objective function is typically defined as the squared error computed at each frequency.

The choice of discretization function for $\gamma(\ln(\tau))$ becomes equally critical for DRT regression. While Tikhonov regularization ensures numerical stability, the discretization scheme determines the accuracy and physical interpretability of the DRT. Among the available methods, Radial Basis Functions (RBFs) have proven more effective than piecewise linear approximations, as they allow control over the trade-off between resolution and smoothness through a shape factor [32]. A practical criterion sets this factor so that the full width at half maximum (FWHM) of each basis function matches the average logarithmic spacing of the experimental frequencies, ensuring both physical consistency and numerical robustness [32]. In this paper, a Gaussian RBF function is employed for the approximation of the logarithmic time constant distribution function.

For DRT regression, to date, there are various open-source tools available to researchers such as: DRTtools by Wan et al. [32], Bayes DRT by Huang et al. [33] and DRT by Kulikovskiy [34]. In this work, an in-house tool was used to calculate the DRT regression which takes inspiration from some of the previously mentioned works.

1.2. Study overview and novelty

Despite the growing interest in DRT analysis, no comprehensive work has systematically examined the DRT spectra of low-temperature PEMFCs across a broad matrix of operating conditions. This study addresses this gap by analyzing more than 150 experimental EIS datasets collected from a single 25 cm² PEMFC and processed using the DRT method extracting important features. The approach avoids preliminary assumptions that could introduce bias, allowing each spectral feature to be rigorously linked to its underlying electrochemical process. To capture the influence of key operating parameters on fuel cell impedance, targeted experiments were designed in which one variable was systematically varied while all others were held constant. The parameters investigated include temperature, pressure, oxidant stoichiometry, oxidant type, and applied load—all of which play critical roles in PEMFC performance. For example, temperature strongly affects ionic conductivity and water management, with typical operating ranges between 25 °C and 85 °C [35,36], while emerging electrolyte materials aim to extend this range up to 120 °C to improve CO tolerance and reaction kinetics [35]. Similarly, pressure impacts open-circuit voltage and overvoltages, but excessive values can lead to hydrogen crossover and mechanical instability [37,38]. Air flowrate and oxidant type further influence mass transport limitations and reaction kinetics [39–41], while load conditions dictate activation resistance and catalyst degradation mechanisms [42,43].

The novelty of this work lies in three main aspects:

1. **Comprehensive Multi-Dimensional Analysis.** The study systematically quantifies how the relative contributions of individual DRT peaks evolve across a wide, interconnected matrix of operating conditions. This goes beyond simple peak identification, enabling a deeper understanding of mechanistic changes under varying loads, temperatures, pressures, and oxidant conditions.
2. **Non-Linear Statistical Framework for Peak Significance.** A non-linear statistical approach is employed to validate whether observed peaks are truly significant and not phantom artifacts. This method reveals complex, non-linear correlations between peak characteristics (resistances and time constants) and operating parameters, providing insights into the mechanistic interplay governing PEMFC behavior.

3. **Assessment of DRT Reconstruction Error.** The average DRT reconstruction error and its confidence intervals across the entire dataset are reported. This analysis highlights that the error is not negligible, raising important considerations for peak interpretation and guiding best practices for managing uncertainty in DRT-based diagnostics.

2. Material and methods

2.1. Testing conditions

In this study, the following operating parameters were systematically varied to assess their influence on the fuel cell's impedance under 100 % RH of reactant gases.

Temperature: from 40 °C to 80 °C with an increment step of 10 °C.

Pressure: for every temperature, the reactant pressure varied from 0 to 2 bar with increments of 0.5 bar.

Flowrate: the air flow rate was adjusted to correspond to three different oxygen stoichiometries: 1 (stoichiometric flow), 2 (ideal flow) and 3 (excess flow). This dependency was investigated under conditions of 80 °C, 0.5 bar and 100 % relative humidity.

Oxidant: the effect of switching to pure oxygen as the oxidant was analyzed under 70 °C, 0.5 bar and 100 % relative humidity conditions.

Cell Voltage: for every temperature and pressure, the cell voltage was adjusted from 0.8 V down to 0.4 V in steps of 0.1 V.

2.2. Single cell preparation

The single cell was prepared in-house using commercial materials. The procedure consisted of the following main steps:

Membrane and catalyst ink preparation. A Nafion 212 membrane (6 × 6 cm, Chemours) in the proton cycle was used in dry state for the deposition of the catalyst layers. The catalyst ink was prepared using HiSPEC4000 (40 wt% Pt on Vulcan XC-72, Johnson-Matthey), Nafion D521 ionomer (Chemours), and a solvent mixture of acetone and isopropanol (1:1 by weight, per analysis, Penta). The solid-to-liquid weight ratio was 1:60, the ionomer-to-carbon weight ratio (I:C) was kept constant at 0.4 and a total volume of 15 cm³ of ink was homogenized using an MS73 ultrasonication probe (Bandelin, 15 W power output) for 10 min in an ice bath. Ink was intensively stirred until deposition itself.

Catalyst layer deposition. The ink was sprayed onto the membrane using a CNC-operated (CZ Robotics) ultrasonic nozzle (Cheersonic) with nitrogen as focusing gas (99.99 vol%, SIAD) of flow rate 50 cm³/min. The membrane was fixed on a hotplate at 60 °C with a 1 mm PTFE mask with an opening 5 × 5 cm². Nozzle was positioned 1 cm above the surface of membrane. Spraying was performed with ink injection speed to nozzle 0.5 cm³ min⁻¹ using linear pump (New Era Pumps) in serpentine geometry with line distance 5 mm and cross-repeating pattern to reach a Pt loading of 0.3 mg cm⁻² on both anode and cathode. Number of required layers was calculated based on ink flow rate and geometry of deposition.

Verification of Pt loading. Selected catalyst-coated membranes (CCMs) were dissolved in Aqua Regia, and the Pt content was quantified by ICP-OES (Optima8000, PerkinElmer).

Membrane hydration. Prior to assembly, CCMs were hydrated in deionized water at 80 °C for 2 h.

MEA assembly. The hydrated CCM was combined with Gas Diffusion Layers (GDLs) and silicon sealings and assembled in a commercial LT-cell (Leancat) pressed with a pneumatic piston at force of 1.25 kN. Graphite endplates with a triple open-end serpentine flow field were employed at both electrodes. Non-woven carbon paper Sigracet 22BB was used as GDLs, with a 5 wt% PTFE-treated microporous layer and a total thickness of 215 μm.

Cell conditioning. The cell was first purified by N₂ at 100 cm³ min⁻¹ for 10 min on both electrodes. Break-in was then performed at 80 °C under H₂/O₂ with stoichiometric overflow (1.5/2.0, respectively),

100 % relative humidity, 0.5 bar overpressure, and 0.5 A cm⁻² current density for at least 12 h, or until voltage stabilization using computer-controlled current load DL3021 (Rigol).

2.3. Test bench set-up

The test station is built in-house and consists of two computer-controlled Elflow mass flow controllers (Bronkhorst), one for hydrogen and the other for oxygen/air. The gas flows are then directed through two separate Nafion tubing-based gas-to-water humidifiers (diameter 1/8", length 24", Permapure) in insulated glass water-filled vessels equipped with silicon-insulated heating elements of power 100 W and K-type thermocouples (Omega Engineering) for precise temperature regulation to set up the desired relative humidity. The reactants subsequently flow through insulated metallic Swagelok 1/8" tubing, also fitted with K-type thermocouples and silicon-insulated heating elements of power 80 W (Omega Engineering) to maintain stable temperatures of gas inlet. Cell is heated using cartridge heaters of power 200 W with K-type thermocouples (Omega Engineering), controlled by PID controllers (Delta Electronics).

2.4. EIS test protocol

The EIS was conducted using ModuLab XM ECS potentiostat with 100 A booster (AMETEK), used in potentiostatic mode. The instrument is coupled with a frequency response analyser device to obtain the impedance at all the frequency of interest. The impedance measurement is carried out for each load after a stabilization period to assure. The test protocol is as follows.

1. Potentiostatic control at 0.5 V for 120 s.
2. Open Circuit Voltage (OCV) for 30 s.
3. Potentiostatic control at target voltage for 120 s.
4. EIS measurement.

Steps 3 and 4 are repeated in a loop to collect the complex impedance of the PEMFC from 0.8 V to 0.4 V in 0.1 V decrements. Details are provided in Table 1.

Impedance data with a negative real part or a positive imaginary part are excluded from the analysis. These occur primarily at high frequencies, resulting in a variable initial frequency from test to test. The experimental impedance data under all operating conditions considered in this study are presented as Nyquist plots in the Supplementary Material.

3. Results and discussions

This section provides a detailed analysis of PEMFC behavior under varying operating conditions using the DRT approach. It begins with polarization curves to highlight the macroscopic effects of temperature, pressure, flow rate, and oxidant composition. The reliability of the DRT results is then assessed through fitting error evaluation, identifying the frequency ranges where the deconvolution is most trustworthy. Finally,

Table 1
EIS measurements set-up.

Parameters	Value	Unit of measurement
Initial voltage bias level	0.8	V
Final voltage bias level	0.4	V
Voltage step	0.1	V
Initial Frequency	100000	Hz
Final Frequency	0.1	Hz
Amplitude (RMS)	±5 %	V
Methodology	Sine frequency swept	-
Frequency swept trend	Exponential	-
Points per decade	18	-

the DRT spectra are examined to track the evolution of relaxation processes and their sensitivity to operating parameters, with trends in extracted resistive contributions analyzed statistically. A physical interpretation of the observed features is offered at the end of the section.

3.1. Polarization curves and performance trends

To provide an initial overview of the influence of both parameters, Fig. 1 presents load curves as a function of pressure and temperature (Fig. 1a), flowrate (Fig. 1b) and oxidant (Fig. 1c). Reactant pressure consistently enhances performance, increasing current density by about 70 % at 80 °C and 50 % at lower temperatures compared to atmospheric pressure. Temperature has a similar positive effect, improving current by roughly 27 % at 2 bar between 40 °C and 80 °C. However, at 80 °C and low pressures (0–1 bar), performance declines relative to 70 °C, likely due to drying at the CL–PEM interface. Excess heat at high temperature and low pressure can dehydrate the membrane, hindering reactant distribution. This effect is further aggravated by the relatively thick Nafion N212 membrane, which can develop stronger internal hydration gradients than ultrathin (~10 μm) membranes [44].

Increasing air flow produces comparable effects: raising stoichiometry from 1 to 2 doubles current density, while further increases give marginal gains. Switching to pure oxygen removes diffusion losses and accelerates kinetics, more than doubling current density at 0.5 V.

3.2. DRT regression error

Applying DRT to PEMFC data requires a clear assessment of its reconstruction accuracy. Before interpreting the extracted processes, we therefore quantify the error between the impedance reconstructed by the nonlinear DRT regression and the experimental spectra. Fig. 2, reports the mean and standard deviation of this error across all tests, along with the average time constants and confidence intervals of the identified peaks. The fitting error is initially high but rapidly decreases, approaching zero around 3 kHz and remaining low down to around 10 Hz, where it increases again due to experimental scattering—reaching up to 20 % for the imaginary part at 0.1 Hz. High-frequency deviations are attributed to the inability of the DRT model to fully capture the experimental impedance trend, particularly affecting peaks P1 and P2. Similarly, data dispersion at low frequencies may introduce uncertainty in the identification of peak P6, though its mean time constant remains

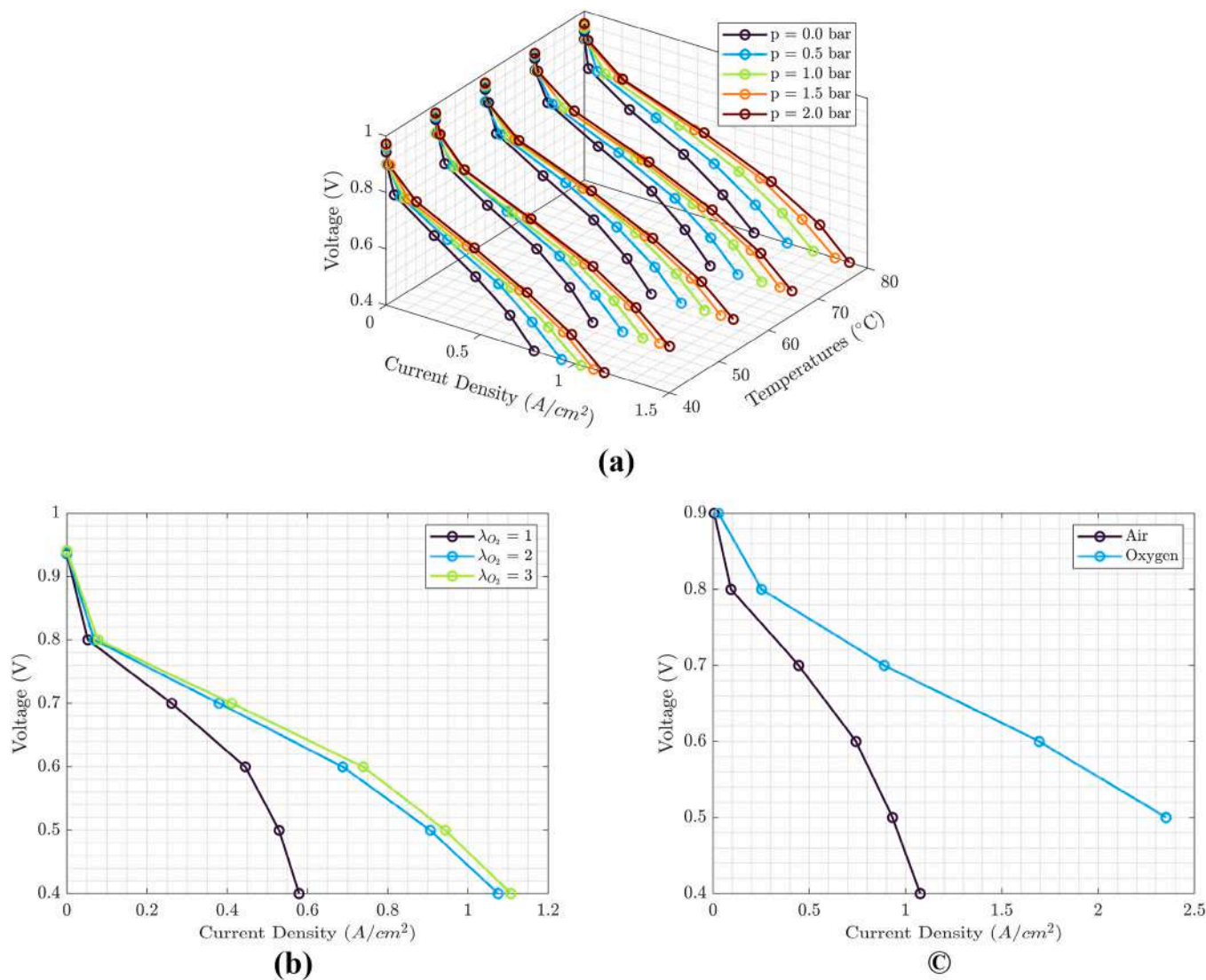


Fig. 1. (a) Static polarization Curves at different temperatures and pressures with fixed mass flowrates (ideal) and RH (100 %). (b) Static polarization Curves at different oxygen stoichiometry at 70 °C, 0.5 bar and 100 % RH. (c) Static polarization Curves with air and pure oxygen at 70 °C, 0.5 bar and 100 % RH and ideal stoichiometries.

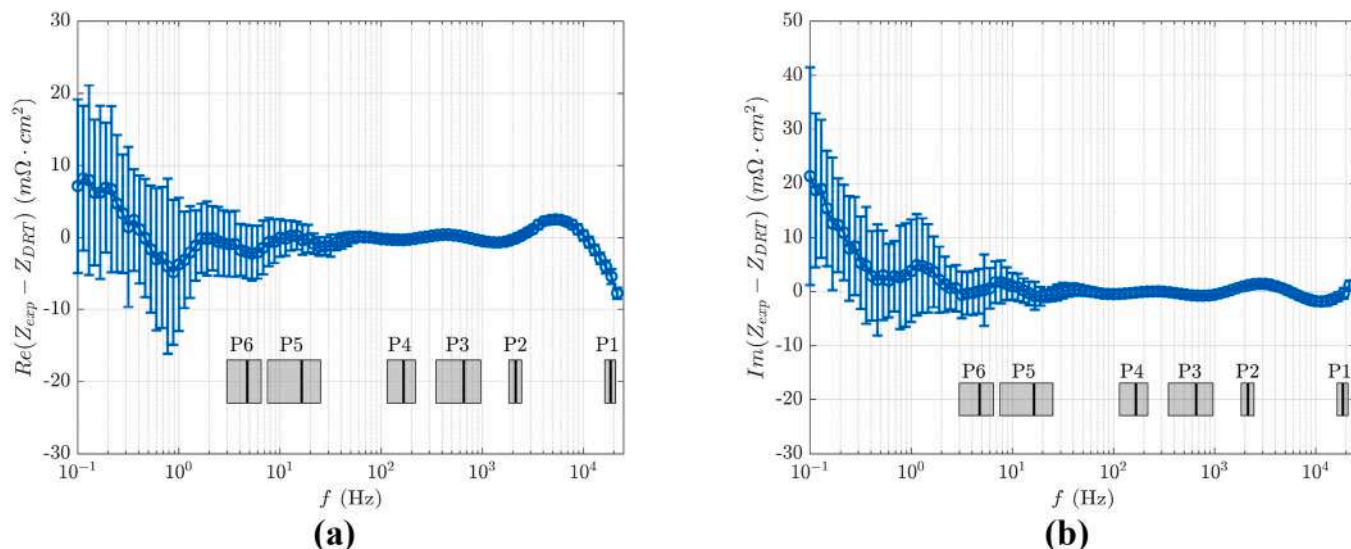


Fig. 2. Residuals of the real (a) and imaginary (b) parts of the impedance, calculated as $(Z_{exp} - Z_{DRT})$ at each frequency, evaluated over the entire dataset. In addition, the grey rectangles indicate the confidence intervals of the time constants associated with the different DRT peaks, while the vertical black lines mark their mean values calculated across the whole dataset.

beyond the range most affected by reconstruction error.

3.3. DRT response across load conditions and influence of operating parameters

This chapter analyzes the DRT response of the PEMFC across a wide range of operating voltages (0.8 V–0.4 V) and evaluates the influence of key parameters — temperature, pressure, flow rate, and oxidant type — on the relaxation behavior of the cell. The objective is to identify how electrochemical and transport processes evolve with increasing load, as well as to isolate the specific effects of each operating variable under different voltage regime.

3.3.1. General trends with load

Fig. 3 presents the DRT spectra at different voltages (0.8–0.4 V) under fixed reference conditions (70 °C, 0.5 bar, $\lambda_{O_2} = 2$, air as oxidant). Six well-defined peaks (P1–P6) are identified, five of which are consistently visible across the full voltage range.

At high frequencies (>10 kHz), P1 exhibits negligible magnitude and remains virtually constant in both resistance and time constant,

indicating no dependence on load.

P2 (~5 kHz) decreases in magnitude with increasing load and shifts toward shorter time constants.

P3, in the intermediate-frequency range (100 Hz–1 kHz), shows a steady decrease in both magnitude and time constant.

P4, dominant at low current densities (~100 Hz), decreases exponentially from 0.8 V to 0.7 V, then rises again at lower voltages, with a mirrored trend in its time constant.

P5 (100–10 Hz) increases monotonically in magnitude as load rises, while its time constant decreases.

Finally, P6 appears only at high loads (<0.5 V) in the very-low-frequency range (10–0.1 Hz), with increasing magnitude and slightly shorter time constants.

These observations reveal three main patterns across the voltage range:

- **Peak emergence:** A new peak (P6) appears under high-load conditions, reflecting the onset of additional processes or transport limitations.
- **Peak shifting:** Several peaks move toward shorter or longer time constants with load, indicating progressive changes in the dominant time scales.
- **Peak stability:** No peaks disappear under the current conditions, although partial overlap among P2–P4 suggests potential merging at lower spectral resolution.

The following sections examine how these behaviour trends evolve under different operating parameters, distinguishing between low, medium, and high overvoltage regimes.

3.3.2. Low overvoltage case (0.8V): impact of temperature, pressure, flowrate and oxidant

At 0.8 V, the fuel cell operates under low-load conditions, where mass transport processes are minimal. The DRT spectra at this voltage provides a baseline for assessing how each operating parameter influences individual relaxation processes in the absence of significant current demand.

Fig. 4, shows DRT response across different operating conditions identifying 5 different peaks.

P1. Remains nearly unaffected by temperature, pressure, flow rate, or oxidant. Its constant magnitude and time constant indicate no link to

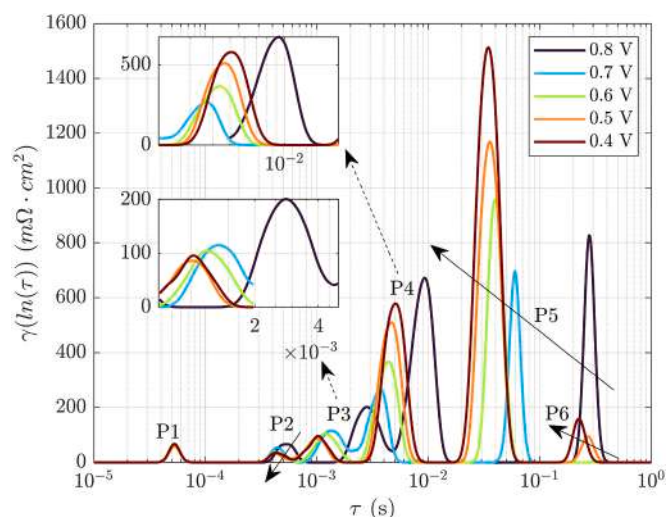


Fig. 3. DRT spectra from 0.8 V to 0.4 V under fixed reference conditions.

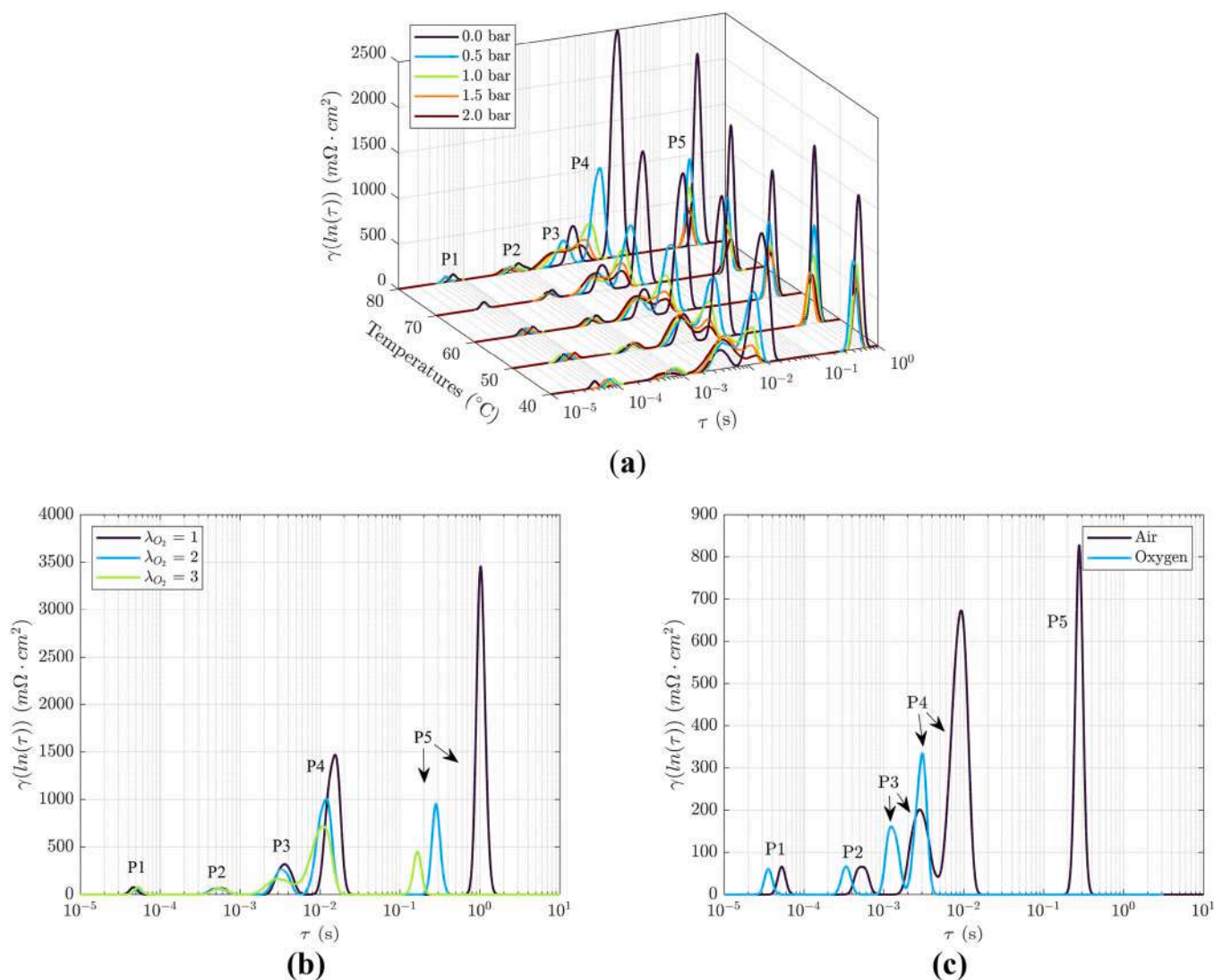


Fig. 4. DRT spectra at 0.8 V under varying operating conditions: (a) temperatures from 80 °C down to 40 °C in 10 °C decrements and pressures from 0 to 2 bar in 0.5 bar steps, at 100 % RH and ideal flow; (b) oxygen stoichiometries from 1 to 3 at 80 °C, 0.5 bar, and 100 % RH; (c) oxidants (air and pure oxygen) at 70 °C, 0.5 bar, and ideal flow.

transport or charge-transfer phenomena. Only pure oxygen operation slightly shifts the peak toward shorter time constants.

P2. Shows negligible amplitude variation but a complex dependence of time constant on temperature and pressure. At 70 °C, increased pressure shortens the time constant while at lower temperatures, the opposite occurs. Under pure oxygen, P2 shifts to shorter time scales, suggesting improved reaction kinetics.

P3. Typically appears as the second or third largest contribution to the impedance spectrum. Under high pressure and high temperature, it decreases in magnitude and shifts toward shorter time constants. At lower temperature (40 °C), this trend reverses: increasing the pressure causes P3 to grow, broaden, and shift to longer time constants. Increasing oxygen stoichiometry has the opposite effect – it lowers P3’s magnitude and accelerates its characteristic time. The same response is observed when switching from air to pure O₂.

P4. Represent one of the primary contributions. Its amplitude and associated time constant are highly sensitive to reactant pressure, exhibiting a pronounced decrease and a concomitant shift toward shorter time constants as pressure increases. In contrast, temperature variations do not produce a consistent qualitative trend. Similar behavior is observed upon increasing oxygen stoichiometry (flow rate) or switching from air to pure O₂, confirming that P4 is governed by the

oxygen concentration at the cathode.

P5. It’s also a primary contributor, its magnitude is highly sensitive to reactant pressure, exhibiting a dramatic decrease as pressure increases, whereas temperature exerts no clear effect. Notably, increasing the flow rate produces an exponential decay in P5’s amplitude, and the peak vanishes entirely under pure O₂, confirming its strong dependence on oxygen concentration at the cathode.

3.3.3. Medium overvoltage case (0.7V–0.6V): impact of temperature, pressure, flowrate and oxidant

At 0.7–0.6 V, the cell transitions toward higher current densities, where ohmic and early diffusion losses emerge. The DRT spectra in Fig. 5 reveal stronger interactions among processes and more pronounced parameter sensitivity.

P1. Remains nearly constant under all operating conditions, confirming its weak dependence on the electrochemical environment.

P2. Gains sensitivity to both temperature and pressure. Increased pressure enhances its magnitude and shifts the time constant to longer values, especially at 0.6 V. At low pressure and high temperature, P2 and P3 tend to merge, forming a broader feature, a trend reinforced under overflow conditions. Pure oxygen increases P2’s magnitude but not its time constant.

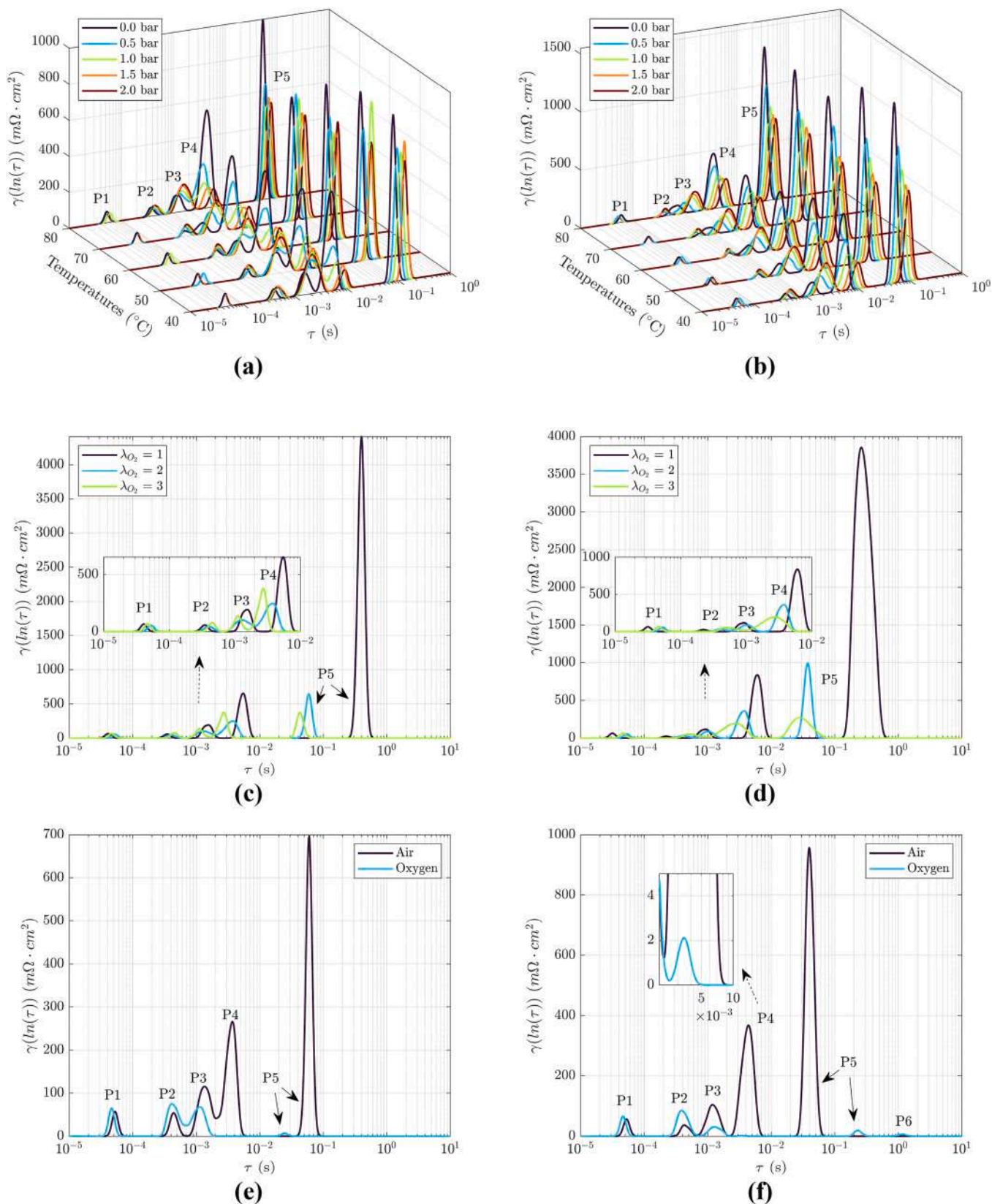


Fig. 5. DRT spectra under varying operating conditions: (a) 0.7V and (b) 0.6V with temperatures from 80 °C down to 40 °C in 10 °C decrements and pressures from 0 to 2 bar in 0.5 bar steps, at 100 % RH and ideal flow; (c) 0.7V and (d) 0.6V and oxygen stoichiometries from 1 to 3 at 80 °C, 0.5 bar, and 100 % RH; (e) 0.7V and (f) 0.6V with different oxidants (air and pure oxygen) at 70 °C, 0.5 bar, and ideal flow.

P3. Its amplitude grows with pressure and decreases with temperature, with corresponding shifts to longer time constants. At 0.6 V, merging with P2 occurs more frequently, especially at zero pressure or under overflow. Raising the flow rate—and likewise using pure O₂—reduces the magnitude of P3, underscoring its sensitivity to oxidant stoichiometry. By contrast, its time constant shortens only with higher flow rate, showing little to no change when switching from air to pure O₂.

P4. Becomes less dominant as pressure increases, with magnitude decreasing and time constant extending. Under pure O₂, P4 nearly disappears at 0.7 V and reappears weakly at 0.6 V, two orders of magnitude smaller, indicating oxygen concentration dependence.

P5. Maintains a major role in the spectrum. Its amplitude decreases with increasing pressure and flow rate, and it nearly vanishes under pure O₂ while temperature maintain a secondary role. The time constant generally increases with pressure and slightly decreases at higher temperature, while operation with pure oxygen shifts it toward even longer values.

P6. Detected only at 0.6 V under pure oxygen, presents a very low amplitude and a long time constant on the order of seconds, possibly reflecting a slow oxygen-related transport phenomenon not evident at higher voltages.

3.3.4. High overvoltage case (0.5V–0.4V): impact of temperature, pressure, flowrate and oxidant

The 0.5 V point corresponds to peak power, with multiple electrochemical and transport contributions becoming strongly activated. Pushing further down to 0.4 V drives the system fully into mass-transport limitation (oxygen starvation, flooding, thermal stress), which is clearly reflected in the DRT response shown in Fig. 6. Pure oxygen measurements at 0.4 V were omitted due to the risk of equipment damage at high current densities.

P1. As at previous voltages, it remains unaffected by changes in operating conditions.

P2. Increases in magnitude under high pressure and temperature, with a consistent shift toward longer time constants. At 0.5 V, P2 merges with P3 under stoichiometric and overflow operation, forming a broader low-amplitude feature that persists and intensifies at 0.4 V.

P3. Its amplitude grows with pressure but diminishes at high temperature (notably at 80 °C), while its time constant increases with both. Flow rate effects are weaker, and P3 tends to merge with P2 under several conditions, becoming secondary to P4 and P5 at high load, especially in air-fed operation.

P4. Exhibits a general decrease in magnitude with increasing pressure, though the trend weakens at elevated temperature. Overflow broadens the relaxation profile, whereas pure O₂ at 0.5 V suppresses amplitude but retains a slight upward trend with increasing load.

P5. Closely mirrors P4. It decreases in amplitude with higher pressure and flow rate and nearly vanishes under pure O₂. At 0.4 V, irregular magnitude trends emerge under high-temperature operation, but time constants shift consistently towards higher values.

P6. Clearly visible at 0.5 V across most conditions, with magnitude increasing under higher pressure and time constant shifting to longer values. Under pure O₂, it persists with slightly lower amplitude and longer relaxation time. At 0.4 V, it appears only under overflow conditions.

3.4. Extracted resistance and time constants evolution

To complement the previous qualitative DRT analysis, the time constants and resistances extracted for each peak will be examined, enabling a more detailed characterization of the cell's internal processes and their response to external factors.

3.4.1. Pressure and temperature evolution at different loads

The time constants of peaks P2–P5, those most representative and

exhibiting substantial variation, are plotted as functions of temperature, pressure, and load in Fig. 7. For P2 (Fig. 7a), the time constant decreases with increasing temperature and decreasing voltage, while pressure generally causes an increase, particularly below 0.8 V. At 0.8 V, fluctuations appear, likely due to flow inhomogeneities at low current densities. The behaviour of P3 (Fig. 7b) is broadly similar with time constants, decreasing with temperature and load but increasing consistently with pressure across most conditions, except at 0.8 V, where minor deviations are observed. Notably, the magnitude of P3 is generally higher than P2, making its trends more robust and less affected by noise. For P4 and P5 (Fig. 7c–d), both peaks exhibit decreasing time constants with increasing temperature and increasing values with pressure, especially below 0.8 V. At 0.8 V, the trend becomes more complex, showing an initial decrease followed by an increase at 2 bar. An exception occurs for P4 at 80 °C, where the decrease with pressure is monotonic. With respect to voltage, P5 shows a continuous reduction in time constant as load increases, while P4 displays a nonlinear behavior—dropping sharply between 0.8 V and 0.7 V, then slightly increasing down to 0.4 V.

Extracted resistance values for the ohmic contribution and for peaks P1–P6 are presented in Fig. 8. The ohmic resistance exhibits a clear exponential dependence on temperature, a well-known result [45], increasing with the lowering of temperature. Reactant pressure, on the other hand, does not have a significant effect at low temperatures but shows a positive impact at higher temperatures. At 80 °C, the 0-bar condition deviates significantly as load increases. This divergence may be due to inefficient reactant distribution and uneven water production, leading to membrane dehydration even under high relative humidity at elevated temperatures [46,47]. Higher pressures seem to mitigate this issue by promoting a more adequately hydrated CL-PEM interface, as evidenced by improved load trends at 80 °C in Fig. 8a. Moreover, the ohmic resistance appears to have a slight dependence on load, with only a barely noticeable increasing trend with the reducing in voltage, this result is in line with theory, as demonstrated by Springer et al. [45].

For the individual peaks, P1 decreases with increasing temperature and pressure, while slightly rising at high load (0.4–0.5 V), though remaining negligible in magnitude. P2 shows a clear increase in resistance with pressure and a mild decrease with temperature; lowering the voltage leads to a small, gradual reduction. P3 follows a similar trend, with resistance decreasing with temperature and increasing with pressure, particularly below 0.8 V. P4 shows the strongest dependence on voltage, with a sharp drop between 0.8 V and 0.7 V followed by a recovery down to 0.4 V. Pressure significantly reduces its resistance, although the effect weakens at high load, while temperature induces a nearly linear decrease. P5 displays a parabolic dependence on load—slightly decreasing between 0.8 V and 0.7 V, then rising steadily at higher currents, becoming dominant at high load. Pressure strongly reduces its resistance in an exponentially saturating manner, while temperature has only a minor influence. Finally, P6 increases in resistance as voltage decreases and slightly at lower temperatures, with no consistent pressure dependence, suggesting complex and condition-dependent behavior.

3.4.2. Stoichiometry and oxidant evolution at different loads

The time constants of the two most significant peaks (P4 and P5) are plotted in Fig. 9 as functions of flow rate (left) and oxidant (right). Increasing the flow rate reduces P4's time constant by approximately 50 % at high voltages, with the most pronounced drop occurring when λ_{O_2} increases from 1 to 2. P5 follows the same pattern but exhibits an almost one-order-of-magnitude decrease in its time constant over the same flow-rate range. Changing the oxygen stoichiometry accelerates P4 at 0.8 V, whereas at 0.5 V the peak reappears at a longer time constant. P5 shows similar behavior: at 0.5 V and 0.4 V its time constant under pure O₂ is nearly an order of magnitude slower than under air.

Fig. 10 presents the resistances extracted for the most responsive peaks, alongside the ohmic resistance, plotted as functions of flow rate

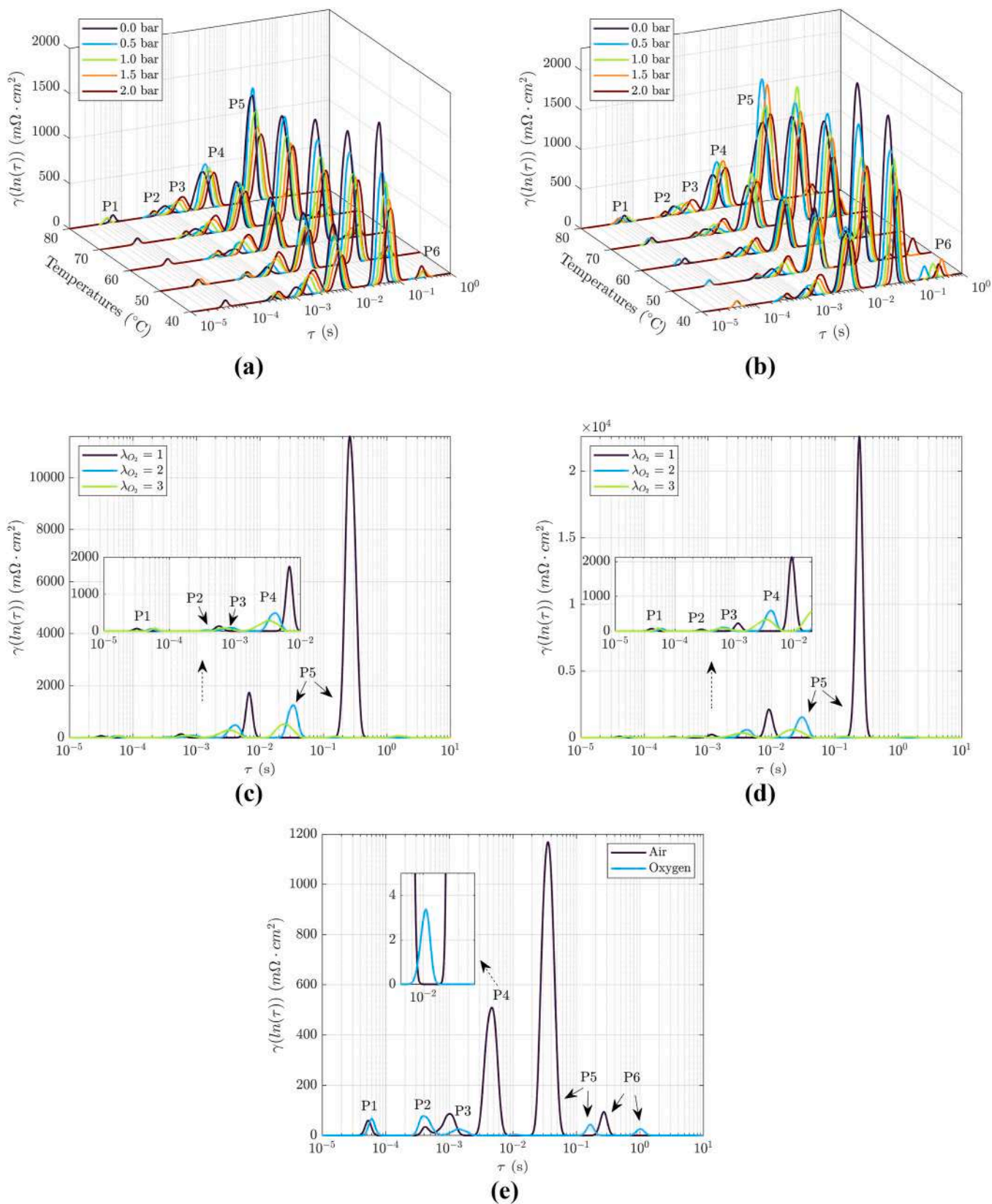


Fig. 6. DRT spectra under varying operating conditions: (a) 0.5V and (b) 0.4V with temperatures from 80 °C down to 40 °C in 10 °C decrements and pressures from 0 to 2 bar in 0.5 bar steps, at 100 % RH and ideal flow; (c) 0.5V and (d) 0.4V and oxygen stoichiometries from 1 to 3 at 80 °C, 0.5 bar, and 100 % RH; (e) 0.5V with different oxidants (air and pure oxygen) at 70 °C, 0.5 bar, and ideal flow.

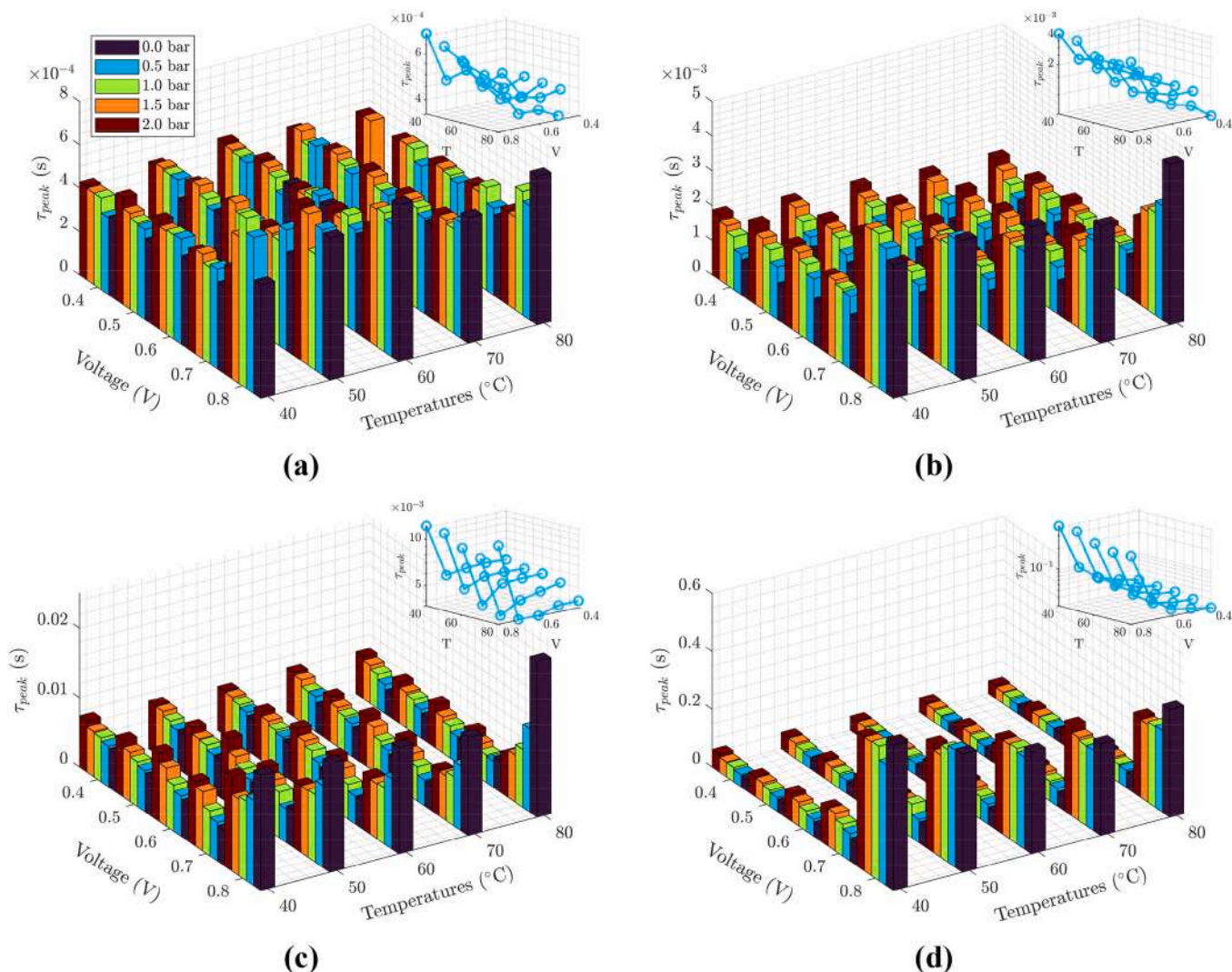


Fig. 7. Peaks time constants: P2 (a), P3 (b), P4 (c), P5 (d), in function of voltage, temperature and pressure. The line graph for each plot refers to peak time constant at 0.5 bar.

and oxidant. It is immediately apparent that the ohmic resistance increases with higher mass flow rates. This behaviour can be attributed to enhanced convective water removal, which dehydrates the electrode interface more effectively, especially under high-load conditions where elevated reaction rates further raise the temperature and accelerate water vaporization. Interestingly, the resistance trend of Peak P1 closely mirrors that of the ohmic contribution, except in the air case during the oxidant comparison (Fig. 10d). In contrast, Peak P4's resistance shows no significant change when the oxygen stoichiometry increases from $\lambda_{O_2} = 2$ to 3, remaining essentially constant despite the more favorable qualitative trends suggested by the DRT spectra. Under pure oxygen, however, P4 reemerges at 0.6 V with a more pronounced increase in resistance, albeit at magnitudes several orders of magnitude lower than in air. Finally, Peak P5 exhibits an exponential decrease in resistance with increasing flow rate, tending toward saturation at high rates. Although its absolute magnitude is lower and it only appears above 0.7 V, P5 displays the same oxidant-dependent behaviour when comparing oxygen to air.

The comparison of P4 and P5 resistances in the oxidant cases (f) and (h) is shown on a logarithmic scale due to their different orders of magnitude.

3.5. Non-linear statistical analysis for extracted resistances

The analysis presented so far has shown that the resistive contributions extracted from the DRT spectra exhibit complex, non-linear behaviours with respect to operating parameters such as temperature, pressure, and cell voltage. These variables often interact in ways that are not immediately intuitive, making it difficult to isolate their individual effects or predict resistance evolution under untested conditions. To better understand these dependencies and quantify the combined influence of multiple parameters, a quadratic regression model (Eq. (2)) was applied to the extracted resistances. This approach enables the identification of both first-order effects (e.g., linear dependence on temperature) and second-order interactions (e.g., temperature–pressure or temperature–voltage coupling), providing a more complete picture of the system's sensitivity and the significance of each peak. The average current during EIS acquisition was used instead of voltage, since current more directly reflects the electrochemical load and the kinetics of internal processes such as the oxygen reduction reaction (ORR) [48].

$$R = a_0 + a_1 i + a_2 T + a_3 P + a_4 i^2 + a_5 T^2 + a_6 P^2 + a_7 iT + a_8 iP + a_9 TP \quad (2)$$

Table 3 summarizes the results of the statistical analysis, reporting the regression coefficients and their corresponding p-values for each

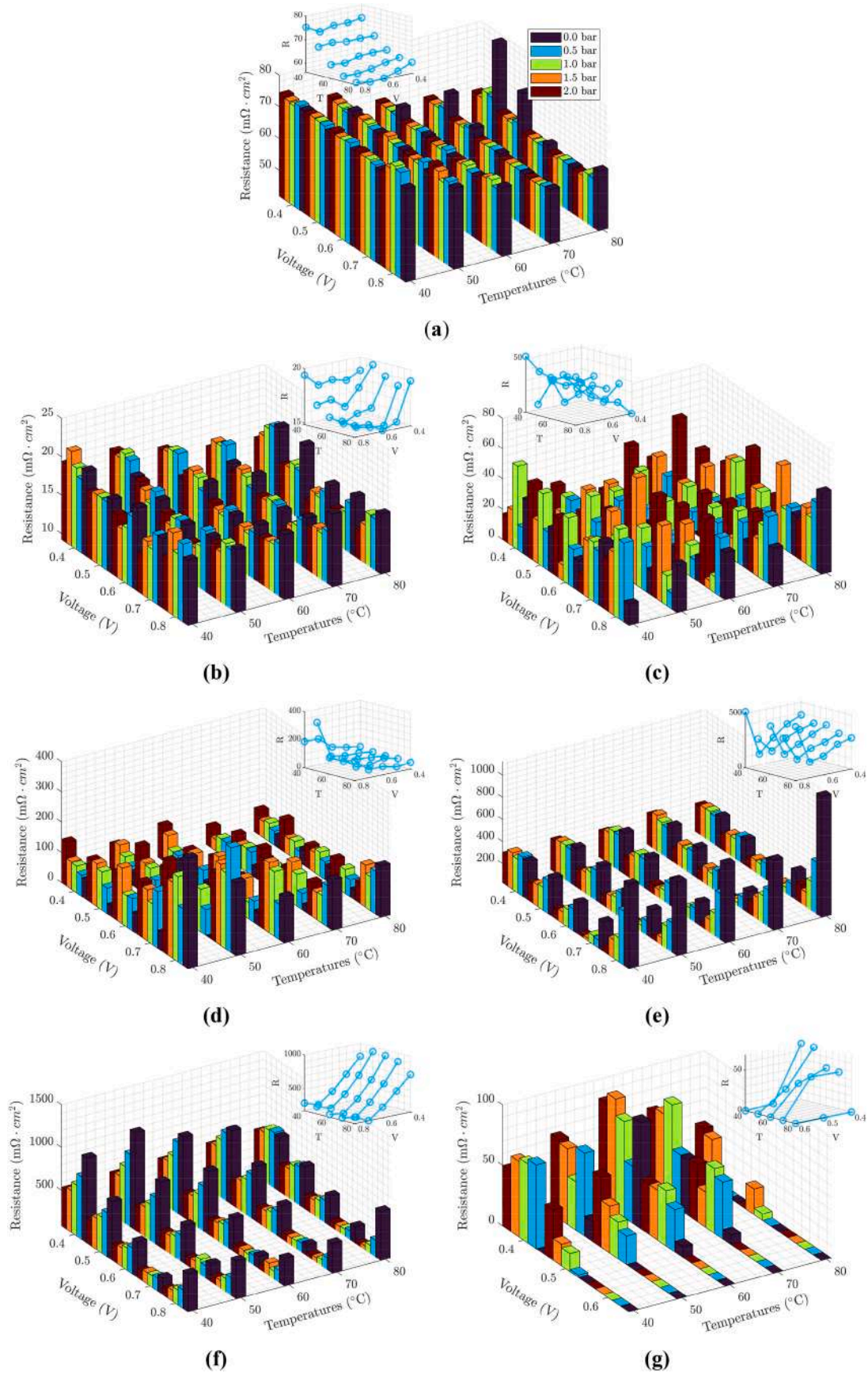


Fig. 8. Resistances for each cluster: Ohmic (a), P1 (b), P2 (c), P3 (d), P4 (e), P5 (f) and P6 (g) as a function of voltage, temperatures and pressures. The line graph for each plot refers to resistance at 0.5 bar.

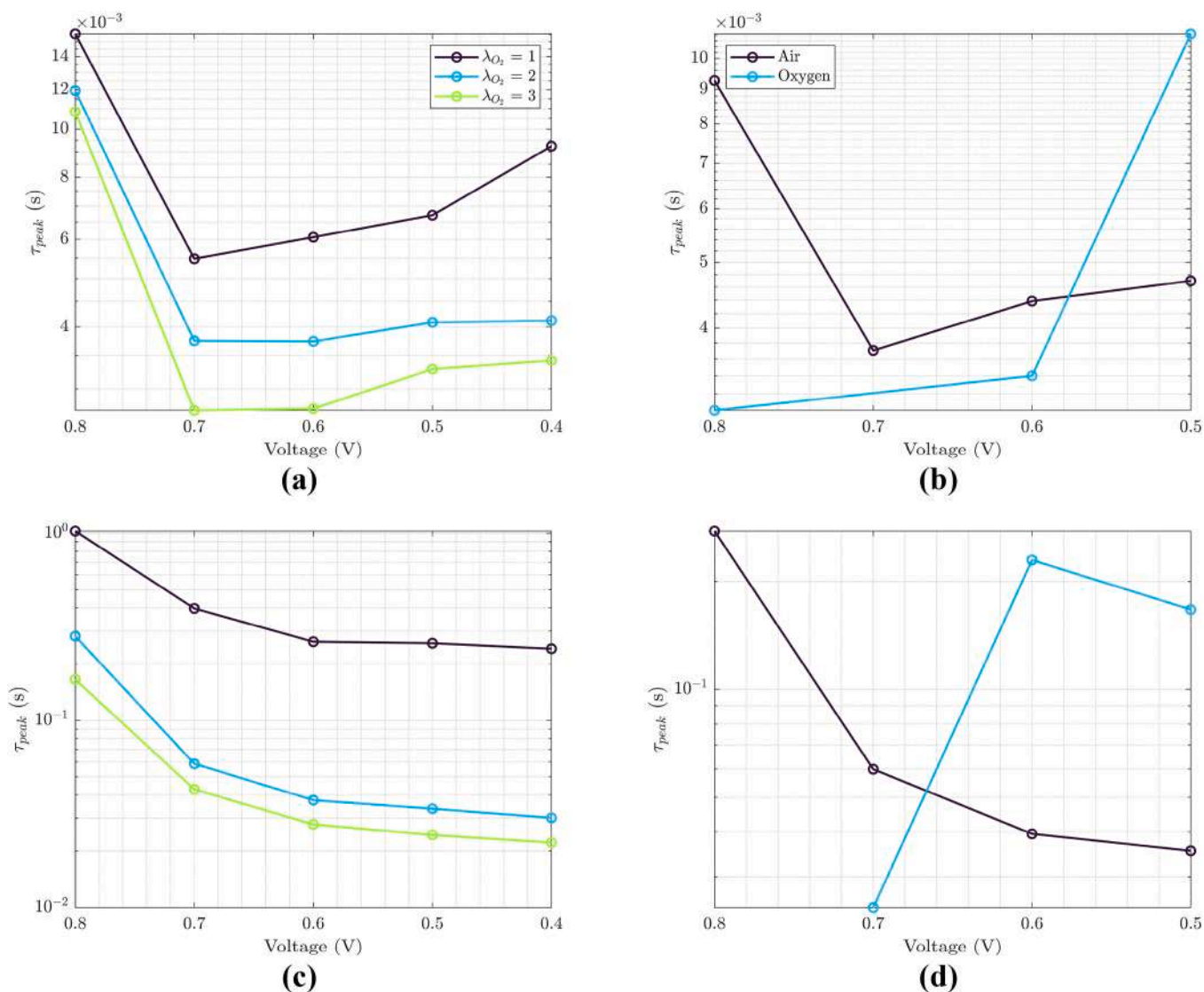


Fig. 9. P4 time constant as a function of voltage for different flowrates (a) and oxidant (b). P5 time constant as a function of voltage for different flowrates (c) and oxidant (d).

peak. The p-value (p) is a key statistical parameter that represents the probability of obtaining results at least as extreme as those observed, assuming the null hypothesis is true. A low p-value (typically below 0.05) indicates that the observed effect is unlikely to be due to random chance and thus supports the alternative hypothesis. A 3-D plot of regression is provided in the Supplementary Material.

The quadratic model explains nearly 90 % of the variance in the ohmic resistance. Both current and temperature have strong nonlinear effects, producing a non-monotonic dependence across the investigated range. Pressure also influences the response, with a convex trend at higher values. All interaction terms are significant, particularly those involving current and pressure, indicating coupled effects that become more evident under high-load conditions. For P1, the model explains about 79 % of the variance. Resistance varies nonlinearly with both current and temperature, while the direct effect of pressure is negligible. However, interactions among the three parameters are statistically relevant, suggesting that combined changes in temperature and pressure can influence this contribution, especially under load. For P2, the model explains only about 20 % of the variance. The dependence on all operating parameters is weak, with only a marginal temperature effect detected. This indicates that the response is poorly captured by the model and may be dominated by local or stochastic variability. The

model for P3 explains roughly 75 % of the variance. The resistance shows a clear nonlinear dependence on current and pressure, while temperature has no significant influence. A mild current–temperature coupling is observed, but other interactions remain negligible. For P4, about 77 % of the variance is captured. Current exerts the strongest influence with a distinct nonlinear trend, while pressure contributes both linearly and quadratically. Temperature has little direct effect, although a small current–temperature interaction is present. Finally, P5 achieves the highest fit quality, explaining more than 90 % of the variance. Resistance depends nonlinearly on both current and pressure, and their mutual interaction is significant. Temperature remains mostly uninformative, but cross-effects among all parameters are still detectable.

3.6. Correlation between resistances and time constants

Despite the complex trends and interdependencies among the operating parameters, it is also important to provide insight into the mutual variation of time constant and resistance. This relationship is particularly relevant from a diagnostic perspective, as the time constant alone may not fully reflect the electrochemical contribution of a given process unless analyzed alongside its associated resistance. Table 3, summarizes the impact of operating conditions on both the time constants and

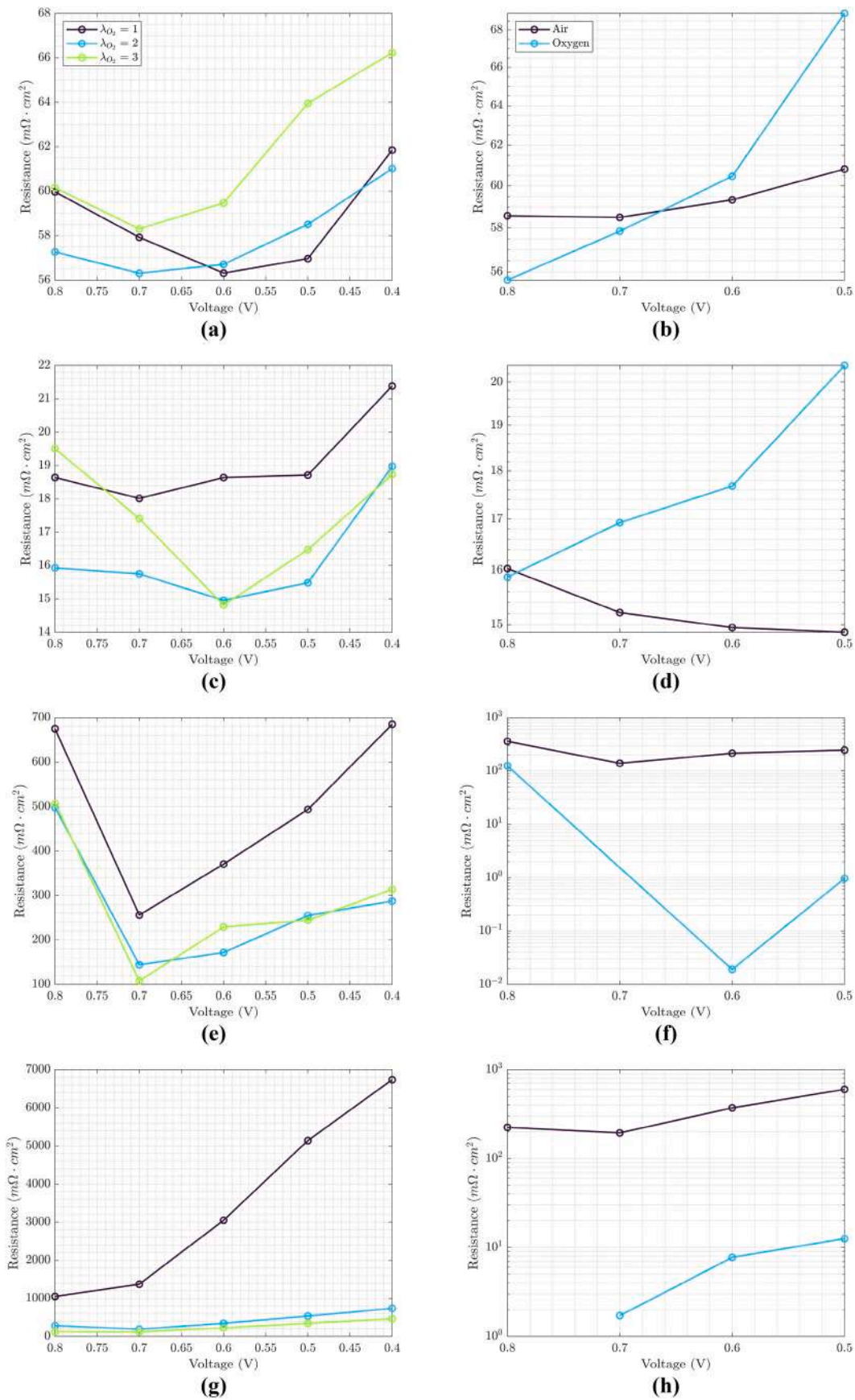


Fig. 10. Ohmic resistance as a function of voltage for different flowrate (a) and oxidant (b). P1 resistance as a function of voltage for different flowrate (c) and oxidant (d). P4 resistance as a function of voltage for different of flowrate (e) and oxidant (f). P5 resistance as a function of voltage for different of flowrate (g) and oxidant (h).

Table 2

Statistical parameters for Ohmic and P1–P5 peaks resistance. For p-Value stand for significant ($p < 0.05$), not significant ($p > 0.05$) and marginal ($p \approx 0.05$).

✓
×
▲

	Ohmic		P1		P2		P3		P4		P5	
	Value	p	Value	p	Value	p	Value	p	Value	p	Value	p
a_1	-5.12	▲	-3.63	✓	-14.6	×	-483	✓	-491	✓	249	▲
a_2	-1.24	✓	-0.268	✓	-1.50	▲	-3.54	×	-4.41	×	-7.27	×
a_3	4.01	✓	0.20	×	8.61	×	111	✓	-310	✓	-392	✓
a_4	5.03	✓	8.56	✓	0.624	×	138.3	✓	753	✓	853	✓
a_5	0.0075	✓	0.0021	✓	0.0118	×	0.007	×	0.0635	×	0.05	×
a_6	1.40	✓	0.331	×	-2.67	×	-8.69	×	48.9	✓	147	✓
a_7	0.080	▲	-0.061	✓	-0.05	×	-3.01	✓	-7.93	✓	-6.74	✓
a_8	-3.39	✓	-1.38	✓	6.07	×	11.8	×	43.1	×	-392	✓
a_9	-0.099	✓	-0.025	✓	0.0286	×	-1.11	✓	0.46	×	1.63	✓
R^2	0.896	-	0.786	-	0.209	-	0.751	-	0.766	-	0.904	-

Table 3

Summary of the trend of resistance and time constant of the peaks P1–P5 in response to changes in voltage, temperature, pressure, or stoichiometry. Symbols indicate the qualitative behavior of a given parameter under variation of an operating condition Specifically: “↑” indicates a monotonic increasing trend, “↓” a monotonic decreasing trend, “U” a parabolic trend characterized by an initial decrease followed by an increase and “-” indicates that no information is extracted.

Peaks	$\Delta V < 0$		$\Delta P > 0$		$\Delta T > 0$		$\Delta \lambda_{O_2} > 0$	
	R	τ	R	τ	R	τ	R	τ
P1	U	-	-	-	↓	↑	-	↑
P2	↓	↓	↑	↑	-	↓	↓	↓
P3	↓	↓	↑	↑	↓	↓	↓	↓
P4	U	U	↓	↑	↓	↓	↓	↓
P5	↑	↓	↓	↑	↓	↓	↓	↓

resistances of the identified peaks. Some notable non-aligned behaviours emerge. For example, peak P1 shows an irregular response in time constant with changing temperature, while peaks P4 and P5 respond to increasing pressure with a clear reduction in resistance but a concurrent increase in time constant. Similarly, for peak P5, decreasing the voltage leads to a shorter time constant but a higher resistance, indicating that the process becomes more prominent while occurring on faster time scales. These observations highlight that a faster process (shorter τ) does not necessarily imply a reduced electrochemical relevance (lower R), underlining the need to consider both dimensions to correctly interpret the underlying dynamics.

3.7. Physical interpretation of DRT peaks

Having extensively presented both the qualitative and quantitative trends of the DRT peaks under varying operating conditions. Sufficient insight is now available to draw conclusions regarding the underlying physical phenomena within the PEMFC to which each peak can be

attributed. The interpretation relies on a combined analysis of each peak’s frequency position, associated resistance, and sensitivity to operating parameters.

Relevant comparisons from the literature are also considered to support the proposed interpretations and provide physical justification. It’s known that the DRT spectrum should not be interpreted without any prior knowledge of the electrochemical system under analysis. From literature, it is known that the total polarization of a PEMFC comprises several contributions [19,25,49,50] namely:

- Hydrogen Oxidation Reaction (HOR).
- Oxygen Reduction Reaction (ORR).
- Proton diffusion in the Catalyst Layers (CLs).
- Oxygen diffusion in the cathode CL.
- Oxygen diffusion in the cathode gas diffusion layer (GDL) and channels (CH).

These phenomena are characterized by different time constants, and attributing the visible peaks in the DRT to these processes is a common practice. Kulikovskiy et al. [51], applied the DRT approach to an analytical model of the cathode of a PEMFC, identifying 5 peaks and associating them as follows: the low-frequency peaks ($5 \cdot 10^0 - 5 \cdot 10^1$ Hz) to O_2 diffusion in the channels (CH), gas diffusion layer (GDL), and catalyst layer (CL), with the latter two combined into a single peak. The intermediate-frequency peak (10^2 Hz) was attributed to the ORR, while the high-frequency peaks ($\geq 10^3$ Hz) were associated with proton diffusion in CL. Han et al. [25], in their study on the application of DRT to PEMFCs, identified five distinct peaks: the one around 10^1 Hz was attributed to O_2 mass transfer, the one near $5 \cdot 10^1$ Hz to the ORR, those in the range of $5 \cdot 10^2 - 2 \cdot 10^3$ Hz to proton diffusion within the catalyst layer, and the highest-frequency peak, around 10^4 Hz, to proton transfer through the membrane. In other studies, such as that by Yuan et al. [52], this high-frequency peak has been attributed to the contact interface resistance between the PEM and the electrode.

In this study, the high frequency peak, P1, is located around 18.5 kHz

and based on the analysis carried out, its time constant shows no dependence on any operating parameter and appears to be primarily influenced by the initial frequency of the DRT analysis, in fact, it often closely matches this starting point. The resistance associated with P1 is marginal compared to the other peaks, though it does exhibit some trends: it decreases linearly with temperature, and shows a non-monotonic dependence on load, decreasing initially and then rising again at high current densities. Nevertheless, because this peak lies in the high-error region of the DRT reconstruction, its interpretation should be approached with caution. We believe that its appearance is largely a result of overshooting in the DRT regression, rather than a signature of a real internal electrochemical process. Indeed, the modeled impedance and the experimental impedance do not perfectly match in the high-frequency range, where the DRT fit tends to shift forward and start from a lower value (see Fig. 2). This discrepancy is reflected also in the ohmic resistance calculated from the DRT, which is consistently higher than the actual resistance measured at the highest frequency point (see Fig. 2a, negative relative error on the real part of impedance). As discussed in the introduction, this fitting error stems from the frequency response of proton diffusion in the catalyst layer, which behaves like a straight line with a theoretical 45° slope (often steeper or distorted in practice). However, we do not consider this peak to be merely an artifact. On the contrary, we argue that its magnitude reflects the linear segment associated with proton diffusion, or may alternatively be associated with the ohmic resistance, since the experimental data often does not start from an imaginary part equal to zero. It can therefore be tentatively linked to this phenomenon, albeit with the acknowledged limitations of the DRT model.

Peak P2 appears in the frequency region around 2.1 kHz. This peak is not consistently observed in the literature, nor is it always present in this study, as it often collapses into Peak P3. Han et al. [25], when observing it, attributed P2, along with P1 and P3, to proton diffusion phenomena within the catalyst layer. However, the trends exhibited by these peaks under varying operating conditions differ significantly, suggesting distinct origins or behaviours. In particular, the resistance associated with P2 displays random or inconsistent trends with respect to load, pressure, and temperature. This instability may also stem from the difficulty in reliably extracting its contribution, as P2 is often very small in magnitude and poorly defined in shape or even merged with P3. A purely qualitative analysis focusing on the effect of load revealed a decline in its magnitude with increasing current, followed by a saturation or even reversal at 0.4 V. Its magnitude was notably larger under high-load and oxygen-fed conditions compared to air, suggesting that above a certain current threshold (which is higher with pure O₂), the peak becomes more pronounced again. Nevertheless, this trend does not clearly emerge in the operating range studied under air, and the corresponding polynomial regression, based on current, pressure, and temperature, shows a very poor fit. Additionally, it is important to note that this peak appears in the frequency region where the DRT reconstruction error oscillate around zero (Fig. 2), which further casts doubt on its physical origin. Taken together, these aspects, its inconsistent resistance trends, weak statistical significance, and overlap with P3, suggest that P2 may not reflect a distinct physical phenomenon. Instead, it may represent a so-called “phantom” peak, an artifact that can arise when the regularization parameter (λ) used in the DRT is too low, allowing noise or fitting artifacts to appear as spurious peaks. However, given that P2 often behaves similarly to P3 and in many cases the two peaks merge, we recommend treating P2's contribution as part of the broader P3-related process when interpreting DRT spectra.

Peak P3 appears in the frequency region around 657.5 Hz and is often associated in the literature with proton diffusion within the catalyst layer (CL) [25,52]. This attribution is primarily based on its relatively fast time constant, consistent with a process occurring in the higher-frequency domain. The time constant of P3 closely follows the trend of its associated resistance, both decreasing with increasing temperature. Additionally, P3 is the only peak whose resistance consistently

decreases as the load increases and increases with rising pressure in most of the tested cases. From a classical perspective, the observed decrease in resistance with temperature is expected, as proton conductivity improves with thermal activation [53]. Its reduction under increasing load could also be interpreted as the result of greater water production at higher current densities, which hydrates the catalyst layer and enhances ionic conduction. However, this interpretation is challenged by the fact that ohmic resistance (see Table 2 and Fig. 8a) shows an overall increasing trend with load, suggesting that at higher current densities the CL may experience drying, possibly due to temperature rise. If proton transport were the limiting factor, both ohmic resistance and P3 would be expected to decrease in a similar fashion, but P3 shows a much stronger current dependence (see Table 2 coefficient a_1 and a_4), pointing to a distinct mechanism. Another non-trivial trend is the influence of pressure, which increases P3's resistance, an effect that becomes less pronounced as pressure approaches 2 bar. Several explanations are possible. One hypothesis is that local pressure build-up leads to morphological changes in the CL, causing anisotropic deformation of ionic pathways. This phenomenon has been reported in studies on clamping pressure [46,54] and can hinder proton transport. Additionally, higher gas-phase pressure reduces the capillary pressure within CL pores, suppressing water condensation. Since proton conductivity depends linearly on liquid water content [55], this effect directly impairs conductivity. Alternatively, the behavior of P3 could suggest a connection to oxygen reduction reaction (ORR)-related steps, particularly given its decreasing trend with load. However, it does not exhibit the typical exponential drop expected for classical ORR resistance. The ORR is a multi-step process: in addition to the direct 4-electron reduction of O₂, a two-step 2-electron pathway may occur, involving adsorbed intermediates such as *O, *OH, and *OOH [56]. These steps require the desorption of water molecules from the surface, which can be hindered at higher pressure, increasing resistance and thereby enhancing the DRT peak magnitude. This interpretation is consistent with studies showing that at high oxygen coverage, the secondary reaction pathway becomes more favorable [57]. Support for this hypothesis also comes from flowrate analysis: increasing the flowrate leads to a notable decrease in P3 resistance, which may be explained by enhanced water removal at the interface. This would facilitate water desorption, promoting reaction turnover, though it would theoretically reduce proton conductivity. Such dual behavior supports a mixed mechanism, where both proton transport and ORR intermediate dynamics may contribute to the observed relaxation.

Peak P4, with an average time constant around 166.7 Hz, is consistently associated with the oxygen reduction reaction (ORR) in the literature [25,51,52], and the trends identified in this work strongly support this assignment. Under pure kinetic control, the ORR resistance is known to vary inversely with current density [58], and this exponential drop is clearly visible in the transition from 0.8 V to 0.7 V with air (Fig. 3). When oxygen is used the peak disappears entirely at 0.7 V and only reappears at 0.6 V and 0.5 V, but with a magnitude several orders of magnitude lower, consistent with the much higher current densities achieved at these voltages in oxygen conditions. No other electrochemical process is expected to produce such a distinct trend. Moreover, the variation of P4 with operating parameters is fully consistent with kinetic expectations: increasing the pressure enhances oxygen availability at the reaction sites, leading to a reduction in resistance across all loads same effect of flowrate increase. Likewise, temperature shows the expected beneficial effect at medium-to-high current densities, but results in a detrimental effect under high-voltage (near-OCV) conditions (Fig. 8e–Table 2, coefficient a_7). This inversion arises because, at low loads, other processes become relevant, such as hydrogen crossover and internal short circuits, which are thermally activated and lead to performance degradation at higher temperatures [37]. As the system moves away from pure kinetic control and mass transport limitations begin to emerge, P4 also increases in magnitude, displaying a clearly nonlinear trend across the full range of voltages and

current densities analyzed. This behaviour has also been reported by Yuan et al. [52], who, in their investigation of internal polarization phenomena, observed a similar evolution of the P4 peak (identified as P2 in their work) using fine current increments, thus capturing the transition in detail. The increase in P4 under high load is attributable to oxygen mass transfer limitations across the cathode compartment layers. In fact, even during standard Tafel slope extraction from polarization curves, a correction is needed in the presence of mass transport limitations to obtain the true kinetic value [59]. It is also well established that under poor CL feeding and high current operation, the observed Tafel slope can double compared to its pure kinetic value [60], clearly indicating the influence of transport effects on the apparent reaction resistance.

Peak P5 appears in the low-frequency region with an average time constant of approximately 16.4 Hz and is widely associated in the literature with oxygen diffusion limitations across the gas diffusion layer (GDL) and catalyst layer (CL) [25,51]. The analyses conducted in this study confirm this assignment. As expected for a mass transport-related phenomenon, P5 is strongly influenced by operating pressure and flowrate, both of which substantially reduce its resistance. Under pure oxygen, the peak disappears entirely, reappearing only at high current densities, and even then, with a much smaller magnitude compared to the other contributions. Within the temperature range analyzed, thermal effects are negligible, as reflected by the lack of statistical significance. In contrast, decreasing the cell voltage leads to a marked increase in P5 resistance, which becomes the dominant feature at high current densities, behaviour that is fully consistent with mass transfer limitations. A seemingly counterintuitive effect is occasionally observed: in some cases, the resistance attributed to mass transport decreases in the transition from 0.8 V to 0.7 V under air, before rising again at lower voltages (Fig. 8f–Table 2 parameter a_4). This trend can be explained by the fact that, at low currents, most of the reaction occurs within small pores due to their high electrochemically active surface area (ECSA) [61]. However, in the CL, oxygen transport is governed by Knudsen diffusion [62] because the mean free path of air is comparable to the pore size [63]. Consequently, if the pores are smaller, the effective oxygen diffusivity worsens, leading to reduced performance. This effect tends to be mitigated with increasing pressure. Moreover, the associated diffusion time constant exhibits an increasing trend with pressure, in line with diffusion theory. As pressure rises, the molecular diffusivity decreases ($D \propto 1/p$), leading to a longer characteristic diffusion time $\tau_{diff} \propto L^2 / D_{eff}$. It is also important to note that, in many studies, this low-frequency peak does not appear at high voltages or low current densities. This behavior is closely linked to oxygen stoichiometry. In the range explored here (stoichiometry 1–3), oxygen concentration progressively decreases along the flow channel due to diffusion into the CL. Consequently, regions farther from the inlet experience local O_2 depletion [64], causing mass transport limitations to appear even under moderate load conditions.

Peak P6, with an average frequency of 4.7 Hz, is typically associated with water transport limitations or water-blocking diffusion effects [25, 50]. This interpretation is consistent with the observations in the present study, and we specifically attribute P6 to mass transfer issues in the gas diffusion layer (GDL) and flow channels (CH) caused by excessive water accumulation. This is evident from the fact that P6 appears only at very low cell voltages, both under air and pure oxygen, conditions corresponding to high water production rates. Its resistance tends to increase with load, but shows no clear trend with other operating parameters, including flowrate. Interestingly, increasing the flowrate can even lead to the appearance of this peak when it was absent at lower stoichiometries. However, these higher stoichiometry cases are also associated with higher current densities, making it clear that current, and thus water generation rate, is the dominant factor influencing the onset of this phenomenon. This interpretation is further supported by the observation that P6 occurs predominantly at high pressure, which not

only increases the overall current but also enhances the differential pressure driving water transport. A higher operating pressure increases the capillary pressure gradient, effectively pushing more liquid water into the GDL and flow channels [61]. In any case, P6 lies in the low-frequency region, where experimental data are often affected by scattering. Therefore, it should be interpreted with caution, as it might partly result from an under-regularized inversion. Although its limited recurrence prevents a statistically robust analysis, low-frequency data scattering is frequently linked to water management instabilities, suggesting that the presence of P6 may still serve as a valuable diagnostic marker.

4. Conclusions

A detailed impedance analysis using DRT has enabled the extraction of information about distinct peaks as a function of key operating parameters, including load, temperature, reactant pressure, flowrate, and oxidant type (air or pure oxygen). This extensive examination of peak resistances and time constants was complemented by statistical modeling to identify which operating parameters significantly influence each feature. This insight was crucial for accurately assigning the peaks to their respective electrochemical processes.

Additionally, the error associated with the nonlinear DRT regression fit was evaluated. It was found that the fitting error decreases sharply below 2 kHz but then rises again in the low-frequency range, raising concerns about the reliability of peak interpretation in this region, particularly for peaks P1 and P6. In fact, Peak P1 ($f_{mean} = 18.5 \text{ kHz}$) appears to be a byproduct of DRT regression overshoot, as its time constant shows no sensitivity to operating conditions. However, its resistance does exhibit some dependence on temperature, suggesting a possible link to proton diffusion in the catalyst layer or to the ohmic contribution, as the experimental data do not start exactly at zero imaginary impedance. Peak P2 ($f_{mean} = 2.1 \text{ kHz}$), located near the transition region where the fitting error approaches zero, may result from oscillations introduced by an overly small regularization parameter. While its qualitative behaviour mirrors that of P3, its extracted resistance is noisy and inconsistent. As such, we recommend merging its contribution with P3 ($f_{mean} = 657.5 \text{ Hz}$), which may correspond to an intermediate step in the ORR pathway, offering an alternative to more conventional interpretations. The final assignment is left to the reader's discretion. In contrast, Peaks P4 ($f_{mean} = 166.7 \text{ Hz}$), P5 ($f_{mean} = 16.4 \text{ Hz}$), and P6 ($f_{mean} = 4.7 \text{ Hz}$) exhibit consistent and well-supported behaviour. They are clearly attributed to, respectively, charge transfer at the interface (ORR kinetics), oxygen diffusion through the CL/GDL, and transport limitations caused by water accumulation that hinders reactant access. Although care must be taken when interpreting peak P6, as it lies in a region affected by higher reconstruction error, this error may in fact originate from actual water management instabilities. Therefore, P6 can still be linked to a water management issue. Overall, these findings highlight the value of DRT analysis as a powerful diagnostic tool for PEMFCs. By resolving overlapping electrochemical processes and providing time-resolved insights, the extracted information can be effectively applied to real-world contexts such as online fault detection, where early deviations can be identified, and operating condition optimization, where parameters can be tuned to maximize performance and durability. The observed trends in extracted parameters provide a comprehensive picture of ohmic losses, ORR kinetics, proton conductivity, and oxygen transport under fully humidified conditions (100 % RH). The same cell has already been analyzed under drying and flooding conditions, with particular attention to the role of pressure and flow rate. A possible future development of this work is the integration of those results with the present analysis, to further investigate the interplay between operating parameters and PEMFC internal dynamics.

CRedit authorship contribution statement

Francesco Mazzeo: Writing – review & editing, Writing – original draft, Visualization, Validation, Supervision, Software, Resources, Project administration, Methodology, Investigation, Formal analysis, Data curation, Conceptualization. **Luca Di Napoli:** Writing – review & editing, Supervision, Software, Resources, Methodology, Conceptualization. **Massimiliana Carello:** Writing – review & editing, Supervision, Resources, Project administration, Conceptualization. **Martin Prokop:** Writing – review & editing, Supervision, Resources, Project administration, Methodology, Conceptualization. **Martin Paidar:** Writing – review & editing, Supervision, Resources, Project administration, Funding acquisition. **Karel Bouzek:** Supervision, Resources, Project administration, Funding acquisition.

Declaration of competing interest

The authors declare that they have no known competing financial interests or personal relationships that could have appeared to influence the work reported in this paper.

Acknowledgments

This publication is part of the project PNRR-NGEU which has received funding from the MUR – DM 352/2022 and from Eaton for the Ph.D. scholarship of author Francesco Mazzeo.

Eaton also supported the research activities.

The experimental activities of this research were supported by the project “The Energy Conversion and Storage”, funded as project No. CZ.02.01.01/00/22_008/0004617 by Programme Johannes Amos Comenius, call Excellent Research.

Appendix A. Supplementary data

Supplementary data to this article can be found online at <https://doi.org/10.1016/j.ijhydene.2025.152860>.

Data availability

The dataset supporting the findings of this study will be openly available at the following link: <https://zenodo.org/records/17278516> with DOI10.5281/zenodo.17278516. It contains all raw impedance measurement data collected by author Francesco Mazzeo during his research stay abroad at the UCTP laboratories. It is provided to support transparency, reproducibility, and further analysis by the research community.

References

- [1] The Paris Agreement | UNFCCC [Online]. Available, <https://unfccc.int/process-and-meetings/the-paris-agreement>. [Accessed 12 December 2024].
- [2] Tashie-Lewis BC, Nnabuife SG. Hydrogen production, distribution, storage and power conversion in a hydrogen economy - a technology review. *Chem Eng J Adv* Nov. 2021;8:100172. <https://doi.org/10.1016/j.cej.2021.100172>.
- [3] Volume Manufacturing of PEM FC Stacks for Transportation and In-line Quality Assurance | VOLUMETRIQ | Project | Fact sheet | H2020 | CORDIS | European Commission. Accessed: February, 17, 2025 [Online]. Available: <https://cordis.europa.eu/project/id/671465>.
- [4] Grano E, Villani M, de Carvalho Pinheiro H, Carello M. Are we testing vehicles the right way? Challenges of electrified and connected vehicles for standard drive cycles and On-Road testing. *World Electric Vehicle Journal* Feb. 2025;16(2):2. <https://doi.org/10.3390/wevj16020094>.
- [5] Mazzeo F, Graziano E, Bodoardo S, Papurello D. Calibration methodology of static, dynamic and ageing parameters of an electrochemical model for a Li-ion cell based on an experimental approach. *Renew Energy* June 2025;246:122793. <https://doi.org/10.1016/j.renene.2025.122793>.
- [6] Carello M, de Carvalho Pinheiro H, Longega L, Di Napoli L. Design and modelling of the powertrain of a hybrid fuel cell electric vehicle, vol. 3; 2021. <https://doi.org/10.4271/2021-01-0734>.
- [7] Guo Z, Grano E, Mazzeo F, de Carvalho Pinheiro H, Carello M. Calibration and validation of a PEM fuel cell hybrid powertrain model for energy management System design. *Designs* Aug. 2025;9(4):94. <https://doi.org/10.3390/designs9040094>.
- [8] Wang S, Zhang J, Gharbi O, Vivier V, Gao M, Orazem ME. Electrochemical impedance spectroscopy. *Nat Rev Methods Primers* June 2021;1(1):1–21. <https://doi.org/10.1038/s43586-021-00039-w>.
- [9] de Levie R. On porous electrodes in electrolyte solutions—IV. *Electrochim Acta* Sept. 1964;9(9):1231–45. [https://doi.org/10.1016/0013-4686\(64\)85015-5](https://doi.org/10.1016/0013-4686(64)85015-5).
- [10] Hong J, Bhardwaj A, Bae H, Kim I, Song S-J. Electrochemical impedance analysis of SOFC with transmission line model using distribution of relaxation times (DRT). *J Electrochem Soc* July 2020;167(11):114504. <https://doi.org/10.1149/1945-7111/aba00f>.
- [11] Grano E, de Carvalho Pinheiro H, Carello M. A novel electric drive description to bridge the gap between energetic and equivalent-circuit models. *Proc Inst Mech Eng - Part D J Automob Eng* May 2025;09544070251330340. <https://doi.org/10.1177/09544070251330340>.
- [12] Ciucci F. Revisiting parameter identification in electrochemical impedance spectroscopy: weighted least squares and optimal experimental design. *Electrochim Acta* Jan. 2013;87:532–45. <https://doi.org/10.1016/j.electacta.2012.09.073>.
- [13] Harrington DA, van den Driessche P. Mechanism and equivalent circuits in electrochemical impedance spectroscopy. *Electrochim Acta* Sept. 2011;56(23):8005–13. <https://doi.org/10.1016/j.electacta.2011.01.067>.
- [14] Chen X, Li L, Liu M, Huang T, Yu A. Detection of lithium plating in lithium-ion batteries by distribution of relaxation times. *J Power Sources* June 2021;496:229867. <https://doi.org/10.1016/j.jpowsour.2021.229867>.
- [15] Yang K, Niu P, Feng Z, Zhu Y, Song Z, Meng J. Rapid acquisition of battery impedance across multiple scenarios using DRT analysis. *J Energy Storage* Nov. 2024;102:114015. <https://doi.org/10.1016/j.est.2024.114015>.
- [16] Zhu J, et al. Low-Temperature separating lithium-ion battery interfacial polarization based on distribution of relaxation times (DRT) of impedance. *IEEE Transactions on Transportation Electrification* June 2021;7(2):410–21. <https://doi.org/10.1109/TTE.2020.3028475>.
- [17] Osinkin DA. Detailed analysis of electrochemical behavior of high-performance solid oxide fuel cell using DRT technique. *J Power Sources* Apr. 2022;527:231120. <https://doi.org/10.1016/j.jpowsour.2022.231120>.
- [18] Subotić V, et al. Detailed insight into processes of reversible solid oxide cells and stacks using DRT analysis. *Energy Convers Manag* Dec. 2020;226:113509. <https://doi.org/10.1016/j.enconman.2020.113509>.
- [19] Nasarre Artigas S, Xu H, Mack F. Use of distribution of relaxation times analysis as an in-situ diagnostic tool for water management in PEM fuel cells applications. *J Power Sources* Apr. 2024;600:234179. <https://doi.org/10.1016/j.jpowsour.2024.234179>.
- [20] Bevilacqua N, et al. Impact of catalyst layer morphology on the operation of high temperature PEM fuel cells. *Journal of Power Sources* Feb. 2021;7:100042. <https://doi.org/10.1016/j.jpowers.2020.100042>.
- [21] Choi W, Shin H-C, Kim JM, Choi J-Y, Yoon W-S. Modeling and applications of Electrochemical Impedance Spectroscopy (EIS) for lithium-ion batteries. *J Electrochem Sci Technol* Jan. 2020;11(1):1–13. <https://doi.org/10.33961/jecst.2019.00528>.
- [22] Hu W, Peng Y, Wei Y, Yang Y. Application of electrochemical impedance spectroscopy to degradation and aging research of lithium-ion batteries. *J Phys Chem C* Mar. 2023;127(9):4465–95. <https://doi.org/10.1021/acs.jpcc.3c00033>.
- [23] Catelani M, et al. Experimental characterization of hybrid supercapacitor under different operating conditions using EIS measurements. *IEEE Trans Instrum Meas* 2024;73:1–10. <https://doi.org/10.1109/TIM.2023.3329094>.
- [24] Kulikovskiy A. Impedance of a PEM fuel cell cathode with nonuniform ionomer loading: analytical and numerical study. *J Electroanal Chem* Mar. 2017;789:174–80. <https://doi.org/10.1016/j.jelechem.2017.02.029>.
- [25] Han L, Shang Y, Liang Q, Liu Y, Guo Z. Distribution of relaxation times used for analyzing the electrochemical impedance spectroscopy of polymer electrolyte membrane fuel cell. *Renew Energy* June 2024;227:120485. <https://doi.org/10.1016/j.renene.2024.120485>.
- [26] Ao Y, Li Z, Laghrouche S, Depernet D, Candusso D, Zhao K. Stack-level diagnosis of proton exchange membrane fuel cell by the distribution of relaxation times analysis of electrochemical impedance spectroscopy. *J Power Sources* May 2024;603:234420. <https://doi.org/10.1016/j.jpowsour.2024.234420>.
- [27] Paul T, Chi PW, Wu PM, Wu MK. Computation of distribution of relaxation times by Tikhonov regularization for Li ion batteries: usage of L-curve method. *Sci Rep* June 2021;11(1):12624. <https://doi.org/10.1038/s41598-021-91871-3>.
- [28] Gavriluk AL, Osinkin DA, Bronin DI. On a variation of the Tikhonov regularization method for calculating the distribution function of relaxation times in impedance spectroscopy. *Electrochim Acta* Sept. 2020;354:136683. <https://doi.org/10.1016/j.electacta.2020.136683>.
- [29] Maradesa A, Py B, Wan TH, Effat MB, Ciucci F. Selecting the regularization parameter in the distribution of relaxation times. *ChemRxiv* Nov. 14, 2022. <https://doi.org/10.26434/chemrxiv-2022-0wb98>.
- [30] Dierckx S, Weber A, Ivers-Tiffée E. How the distribution of relaxation times enhances complex equivalent circuit models for fuel cells. *Electrochim Acta* Sept. 2020;355:136764. <https://doi.org/10.1016/j.electacta.2020.136764>.
- [31] Reshetenko T, Kulikovskiy A. Understanding the distribution of relaxation times of a low-Pt PEM fuel cell. *Electrochim Acta* Sept. 2021;391:138954. <https://doi.org/10.1016/j.electacta.2021.138954>.
- [32] Wan TH, Saccoccio M, Chen C, Ciucci F. Influence of the discretization methods on the distribution of relaxation times deconvolution: implementing radial basis functions with DRTtools. *Electrochim Acta* Dec. 2015;184:483–99. <https://doi.org/10.1016/j.electacta.2015.09.097>.

- [33] Huang J, Papac M, O'Hayre R. Towards robust autonomous impedance spectroscopy analysis: a calibrated hierarchical Bayesian approach for electrochemical impedance spectroscopy (EIS) inversion. *Electrochim Acta* Jan. 2021;367:137493. <https://doi.org/10.1016/j.electacta.2020.137493>.
- [34] Kulikovskiy A. PEM fuel cell distribution of relaxation times: a method for the calculation and behavior of an oxygen transport peak. *Phys Chem Chem Phys* Sept. 2020;22(34):19131–8. <https://doi.org/10.1039/D0CP02094J>.
- [35] Lochner T, Kluge RM, Fichtner J, El-Sayed HA, Garlyyev B, Bandarenka AS. Temperature effects in polymer electrolyte membrane fuel cells. *Chemelectrochem* 2020;7(17):3545–68. <https://doi.org/10.1002/celec.202000588>.
- [36] Ferraris A, et al. Nafion® tubing humidification System for polymer electrolyte membrane fuel cells. *Energies* Jan. 2019;12(9):1773. <https://doi.org/10.3390/en12091773>.
- [37] Mazzeo F, Di Napoli L, Carello M. Assessing open circuit voltage losses in PEMFCs: a new methodological approach. *Energies* Jan. 2024;17(11):11. <https://doi.org/10.3390/en17112785>.
- [38] Hoeflinger J, Hofmann P. Air mass flow and pressure optimisation of a PEM fuel cell range extender system. *Int J Hydrogen Energy* Oct. 2020;45(53):29246–58. <https://doi.org/10.1016/j.ijhydene.2020.07.176>.
- [39] Kim B, Cha D, Kim Y. The effects of air stoichiometry and air excess ratio on the transient response of a PEMFC under load change conditions. *Appl Energy* Jan. 2015;138:143–9. <https://doi.org/10.1016/j.apenergy.2014.10.046>.
- [40] Wang Y, Wang Y. Pressure and oxygen excess ratio control of PEMFC air management system based on neural network and prescribed performance. *Eng Appl Artif Intell* May 2023;121:105850. <https://doi.org/10.1016/j.engappai.2023.105850>.
- [41] Carello M, Landolfi S, Rizzello A, Khadilkar S. CFD analysis of fuel cell humidification System for automotive application. Presented at the WCX SAE World Congress experience, SAE International. Apr. 2023. <https://doi.org/10.4271/2023-01-0493>.
- [42] Fink C, Edjokola JM, Telenta M, Bodner M. Modeling of catalyst degradation in polymer electrolyte membrane fuel cells applied to three-dimensional computational fluid dynamics simulation. *Fuel Cells* 2024;24(5):e202300237. <https://doi.org/10.1002/fuce.202300237>.
- [43] Okonkwo PC. Proton exchange membrane fuel cell catalyst layer degradation mechanisms: a succinct review. *Catalysts* Jan. 2025;15(1):97. <https://doi.org/10.3390/catal15010097>.
- [44] Adachi M, Navessin T, Xie Z, Li FH, Tanaka S, Holdcroft S. Thickness dependence of water permeation through proton exchange membranes. *J Membr Sci* Nov. 2010;364(1):183–93. <https://doi.org/10.1016/j.memsci.2010.08.011>.
- [45] Springer TE, Zawodzinski TA, Gottesfeld S. Polymer electrolyte fuel cell model. *J Electrochem Soc* Aug. 1991;138(8):2334. <https://doi.org/10.1149/1.2085971>.
- [46] Casciola M, Alberti G, Sganappa M, Narducci R. On the decay of Nafion proton conductivity at high temperature and relative humidity. *J Power Sources* Nov. 2006;162(1):141–5. <https://doi.org/10.1016/j.jpowsour.2006.06.023>.
- [47] Karimi MB, Mohammadi F, Hooshyari K. Recent approaches to improve nafion performance for fuel cell applications: a review. *Int J Hydrogen Energy* Nov. 2019;44(54):28919–38. <https://doi.org/10.1016/j.ijhydene.2019.09.096>.
- [48] Impedance analysis of electrochemical systems [Online]. Available, https://pubs.acs.org/doi/epdf/10.1021/acs.chemrev.1c00876?ref=article_openPDF. [Accessed 7 May 2025].
- [49] Napoli LD, Mazzeo F. Health and condition monitoring tool for real-time and on-board diagnosis of PEM fuel cell in heavy duty vehicles. SAE International. Warrendale, PA: SAE Technical Paper 2025-01–8556; Apr. 2025. <https://doi.org/10.4271/2025-01-8556>.
- [50] Heinzmann M, Weber A, Ivers-Tiffée E. Advanced impedance study of polymer electrolyte membrane single cells by means of distribution of relaxation times. *J Power Sources* Oct. 2018;402:24–33. <https://doi.org/10.1016/j.jpowsour.2018.09.004>.
- [51] Kulikovskiy A. A model-based analysis of PEM fuel cell distribution of relaxation times. *Electrochim Acta* Oct. 2022;429:141046. <https://doi.org/10.1016/j.electacta.2022.141046>.
- [52] Yuan H, Dai H, Ming P, Wang X, Wei X. Quantitative analysis of internal polarization dynamics for polymer electrolyte membrane fuel cell by distribution of relaxation times of impedance. *Appl Energy* Dec. 2021;303:117640. <https://doi.org/10.1016/j.apenergy.2021.117640>.
- [53] Du CY, Shi PF, Cheng XQ, Yin GP. Effective protonic and electronic conductivity of the catalyst layers in proton exchange membrane fuel cells. *Electrochem Commun* May 2004;6(5):435–40. <https://doi.org/10.1016/j.elecom.2004.02.006>.
- [54] Borup R, et al. Scientific aspects of polymer electrolyte fuel cell durability and degradation. *Chem Rev* Oct. 2007;107(10):3904–51. <https://doi.org/10.1021/cr050182l>.
- [55] Sun Y, Kadyk T, Kulikovskiy A, Eikerling M. The effect of liquid saturation transients on PEM fuel cell impedance: inductive loop and instability of catalyst layer operation. *J Electrochem Soc* July 2024;171(7):074506. <https://doi.org/10.1149/1945-7111/ad5efd>.
- [56] Luo M, Koper MTM. A kinetic descriptor for the electrolyte effect on the oxygen reduction kinetics on Pt(111). *Nat Catal* July 2022;5(7):615–23. <https://doi.org/10.1038/s41929-022-00810-6>.
- [57] Cheng M, et al. Technical challenges and enhancement strategies for transitioning PEMFCs from H2-air to H2-O2. *Energy Convers Manag* July 2024;311:118525. <https://doi.org/10.1016/j.enconman.2024.118525>.
- [58] Bard AJ, Faulkner LR, White HS. *Electrochemical methods: fundamentals and applications*. John Wiley & Sons; 2022.
- [59] Wang JX, Uribe FA, Springer TE, Zhang J, Adzic RR. Intrinsic kinetic equation for oxygen reduction reaction in acidic media: the double Tafel slope and fuel cell applications. *Faraday Discuss* Oct. 2008;140(0):347–62. <https://doi.org/10.1039/B802218F>.
- [60] Kulikovskiy AA. The regimes of catalyst layer operation in a fuel cell. *Electrochim Acta* Sept. 2010;55(22):6391–401. <https://doi.org/10.1016/j.electacta.2010.06.053>.
- [61] Reshetenko T, Sun Y, Kadyk T, Eikerling M, Kulikovskiy A. An impedance spectroscopy study to unravel the effect of water on proton and oxygen transport in PEM fuel cells. *Electrochim Acta* Dec. 2024;507:145172. <https://doi.org/10.1016/j.electacta.2024.145172>.
- [62] Wang Y, Wang S, Liu S, Li H, Zhu K. Three-dimensional simulation of a PEM fuel cell with experimentally measured through-plane gas effective diffusivity considering Knudsen diffusion and the liquid water effect in porous electrodes. *Electrochim Acta* Sept. 2019;318:770–82. <https://doi.org/10.1016/j.electacta.2019.06.120>.
- [63] Shojaeefard MH, Molaeimanesh GR, Nazemian M, Moqaddari MR. A review on microstructure reconstruction of PEM fuel cells porous electrodes for pore scale simulation. *Int J Hydrogen Energy* Nov. 2016;41(44):20276–93. <https://doi.org/10.1016/j.ijhydene.2016.08.179>.
- [64] Kulikovskiy AA. Chapter 4 - Quasi-2D model of a fuel cell. In: Kulikovskiy AA, editor. *Analytical modelling of fuel cells*. Amsterdam: Elsevier; 2010. p. 117–92. <https://doi.org/10.1016/B978-0-444-53560-3.00009-5>.